A bed pressure correction of the friction term for depth-averaged granular flow models

François Bouchut, Juan Manuel Delgado-Sánchez, Enrique Domingo Fernández-Nieto, Anne Mangeney, Gladys Narbona-Reina

A bed pressure correction of the friction term for depth-averaged granular flow models

F. Bouchut[1], J.M. Delgado-Sánchez[2], E.D. Fernández-Nieto *
Anne Mangeney[3,4], G. Narbona-Reina[2]

March 7, 2022

Abstract

Depth-averaged models, such as the Savage-Hutter model with Coulomb or Pouliquen friction laws, do not in some cases preserve the physical threshold of motion. In particular, the simulated granular mass can start to flow (or stay at rest) even if the slope angle of its free surface is lower (or higher) than the repose angle of the granular material involved. The problem is related to the hydrostatic pressure assumption, associated with the direction of integration, which is orthogonal to a reference plane or a reference bottom. We propose here an initial method to correct this misleading behavior. Firstly, we define a correction of the friction term that accounts for the Jacobian of a change of coordinates, making it possible to reproduce the physical threshold of motion and thus the solutions at rest. Secondly, we observe that the 3D model presented in [F. Bouchut, I. Ionescu, and A. Mangeney. *An analytic approach for the evolution of the static-flowing interface in viscoplastic granular flows. Commun, Math. Sci.*, 14(8):2101–2126, 2016] verifies the physical thresholds of motion because it is based on a second order correction of the pressure valid for slow granular flows. The correction proposed here ensures that the model preserves, up to the second order, the physical threshold of motion defined by the repose angle of the material. Several numerical tests are presented to illustrate certain problems related to classical depth averaged models and the remedial effect of the proposed correction, in particular through comparisons with experimental data. We finally show that this correction is not exact far from the starting and stopping phases of the granular avalanche and should be improved by adding other second order terms in the pressure approximation.

*Departamento de Matemática Aplicada I, Universidad de Sevilla.E.T.S. Arquitectura. Avda, Reina Mercedes, s/n. 41012 Sevilla, Spain (edofer@us.es)

[1]Laboratoire d'Analyse et de Mathématiques Appliquées (UMR 8050), CNRS, Univ. Gustave Eiffel, UPEC, F-77454, Marne-la-Vallée, France (francois.bouchut@univ-eiffel.fr)

[2] Departamento de Matemática Aplicada I, Universidad de Sevilla.E.T.S. Arquitectura. Avda, Reina Mercedes, s/n. 41012 Sevilla, Spain (jmdelga@us.es, gnarbona@us.es)

[3] Université Paris Diderot, Sorbone Paris Cité, Institut de Physique du Globe de Paris, Equipe de Sismologie, 1 rue Jussieu, 75005 Paris, France (mangeney@ipgp.jussieu.fr)

[4] ANGE team, INRIA, CETMEF, Lab. J. Louis Lions, Paris, France

Contents

1 Introduction

Because of their low computational cost, **depth-averaged shallow models** are often used to describe gravitational granular flows at laboratory and field scales, based on the pioneering model proposed by Savage & Hutter [1]. In this model, the flow is assumed to be thin in the direction normal to the topography compared to its length along the slope. To implement this approximation, *local coordinates* are introduced, associated with a reference plane following the slope, and the governing equations are averaged in the direction perpendicular to this plane. In depth-averaged shallow models, the rheology is reduced to the friction boundary condition at the bottom, i.e. at the interface between the base of the granular layer and the topography. This so-called basal friction law must be consistent with the rheology of the granular material involved.
Despite extensive work, the definition of rheological laws for granular materials is still an open issue [2]. The simplest law describing granular flows is based on the Coulomb friction law that describes both the resistance due to friction during the flow and the threshold of motion [1]. These laws imply that

$$\begin{array}{ll} \tau = -\tau_c \operatorname{sgn}(u) & \text{if } |\tau| \geq \tau_c, \\ u = 0 & \text{otherwise,} \end{array} \quad \text{where } \tau_c = \mu\, |\sigma_n| \quad \text{and} \quad \operatorname{sgn}(u) = \frac{u}{|u|}, \tag{1}$$

where u is the velocity of the granular material and σ the stress tensor. Then, if the material flows, the shear stress τ is proportional to the normal stress σ_n through a friction coefficient μ that depends on the nature of the granular material involved and, when applied at the flow/topography boundary, on the nature of this interface (e.g. roughness).

An important characteristic of the behavior of granular materials is the hysteresis that occurs near the transition between flowing and static states. This is observed in particular for a granular layer of thickness h on an inclined plane. If this layer is initially at rest, in order to make the material flow, the inclination angle of the plane has to be increased up to a critical angle θ_{start} (also called the *avalanche angle*). To make the flow stop, this inclination has to be decreased down to a lower critical angle θ_{stop} (the *repose angle*), i.e. $\theta_{stop} < \theta_{start}$. In between these two angles hysteretic behavior is observed. Laboratory experiments show that these angles depend on the thickness of the granular layer [3, 4, 5]. This dependence is weak for large thicknesses (more than 20 times the grain diameter) and very strong for shallow layers for which θ_{stop} and θ_{start} strongly increase as the layer thickness h decreases [3, 2]. Associated *static* and *dynamic* friction coefficients, describing the threshold of motion, can be defined: $\mu_{start} = \tan(\theta_{start})$ and $\mu_{stop} = \tan(\theta_{stop})$.

The so-called $\mu(I)$-rheology, introduced experimentally in [6] and defined by Jop *et al.* in [7], is widely used because of its simplicity and its capacity to reproduce many experimental results. This law defines the internal friction coefficient μ in (1) in terms of the dimensionless number I (ratio of the characteristic time for microscopic rearrangements to the characteristic time for macroscopic deformations). This number, called *inertial number* in [8], and the associated friction coefficient are defined as follows:

$$I = \frac{d\,\dot{\gamma}}{\sqrt{p/\rho_g}}; \qquad \mu(I) = \mu_1 + \frac{\mu_2 - \mu_1}{I_0 + I} I, \tag{2}$$

where $\dot{\gamma}$ is the shear rate, p is the pressure, and d and ρ_g the diameter and density of the grains, respectively. The constant parameters I_0, μ_1 and μ_2 ($\mu_1 < \mu_2$) depend on the granular material involved [7].

Note that for inertial numbers close to zero, $\mu(I)$ reduces to μ_1 which is the minimum value of the friction coefficient and can thus be considered as the threshold of motion (see equation (1)). The hysteresis behavior and the dependence of the threshold on the layer thickness are not considered in the $\mu(I)$-rheology. This is one of the limitations of this rheological law [2].

The hysteresis detailed above has been empirically described in the **basal friction law** proposed by [9, 3], deduced from laboratory experiments for depth-averaged models. The basal friction law is based on equation (1) applied at the base of the flow with a basal friction coefficient $\mu = \mu_b = \mu_P$ that depends on the velocity u and on the thickness h of the flow. This friction coefficient is defined for different regimes based on the values of the Froude number $\mathrm{Fr} = \frac{|u|}{\sqrt{gh}}$,

$$\begin{aligned} &\text{If } \mathrm{Fr} > \beta : && \mu_P = \mu_{stop}\left(h\frac{\beta}{\mathrm{Fr}}\right), \\ &\text{if } 0 \le \mathrm{Fr} \le \beta : && \mu_P = \mu_{start}\,(h) + \left(\frac{\mathrm{Fr}}{\beta}\right)^{\gamma}\big(\mu_{stop}(h) - \mu_{start}(h)\big), \end{aligned} \tag{3}$$

with

$$\mu_{stop}(h) = \tan\delta_1 + (\tan\delta_2 - \tan\delta_1)\frac{1}{1+\frac{h}{L}}; \qquad \mu_{start}(h) = \tan\delta_3 + (\tan\delta_2 - \tan\delta_1)\frac{1}{1+\frac{h}{L}}.$$

The friction angles δ_1, δ_2, δ_3 and the values of the parameters involved are measured empirically for glass beads [3]: $\beta = 0.136$, $L = 0.65$mm, $\gamma = 10^{-3}$, $\delta_1 = 21^{\circ}$, $\delta_2 = 30.7^{\circ}$, $\delta_3 = 22.2^{\circ}$.

This model allows the granular mass to flow when the threshold related to the static friction coefficient μ_{start} is reached and to stop for the threshold related to μ_{stop} (see also [4, 5]). This basal friction law is also compatible with the $\mu(I)$-rheology for the regime $\mathrm{Fr} > \beta$ when steady uniform flows occur. The previous $\mu(I)$ model can be matched for particular choices of the parameters I_0 and L where the angles δ_1 and δ_2 correspond respectively to the coefficients μ_1 and μ_2 in (2), (see [10] for details). As a result, this empirical law describes key processes that are not accounted for in the simpler Coulomb friction law with a constant basal friction coefficient

$$\mu_b = \mu_C = \tan\delta_0, \tag{4}$$

as used in the pioneer Savage & Hutter model [1]

As already mentioned, numerical models for gravitational flows based on the shallow approximation (i.e. hydrostatic pressure) have been shown to provide reasonable results when compared to laboratory and field observations [11]. As these shallow models are used extensively to simulate lab-experiments and assess hazards related to real landslides, it is crucial to fully understand their limitations in order to quantify the associate errors and identify new directions for model improvement.

Because of their simplicity and low computational cost, these models are often applied to granular flows that are not always suitable for the shallow approximation. For example, in a dam-break situation or for real landslides, the released mass may not be shallow at the initial instants, involving strong non-hydrostatic effects [12, 13]. In these situations, shallow models are known to overestimate the flow velocity even though they capture well the final deposit shape and runout distance [14]. Furthermore, even if the flow is shallow, this approximation may not be suitable during the stopping phase. Indeed, other terms may then become important, for example additional terms in the pressure derivation involving thickness gradients [15]. These terms, leading to non-hydrostatic pressures are neglected in the first order asymptotic approximation, $\mathcal{O}(\varepsilon)$, where ε is the typical shallow thickness/length ratio. In the classical asymptotic analysis, it is assumed that μ_b is of order ε^{γ} for some $\gamma > 0$. This assumption and the hydrostatic pressure approximation make it possible to approximate the Coulomb friction term up to $\mathcal{O}(\varepsilon^{1+\gamma})$. Nevertheless, note that when μ_b is of order one, $\mathcal{O}(1)$, which is generally the case, it is necessary to consider higher order approximations of the bed pressure in the definition of the Coulomb

friction term [16].

In this paper, we focus on how shallow models tackle the threshold of motion in granular flows over sloping beds and we identify the key misleading behaviors of such models. The motion criterion ensures that the material flows when the driving forces − gravity, pressure gradients and inertia − exceed the friction force related to the Coulomb threshold (see equation (1)) [4, 5]. When the flow is not uniform, the thickness gradient (i.e. hydrostatic pressure gradient) may play a significant role in the force balance, especially during the starting phase, near the front or during the stopping phase [4]. We show here that shallow (i.e. hydrostatic) models based on the integration of the equations in the direction normal to the topography fail to describe the motion threshold in certain situations. For example, the material may start to flow even if its surface gradient is smaller than the avalanche angle. This problem is related to the approximation of the bed pressure in the definition of the Coulomb friction term, which modifies the motion criterion. As presented in [15], a second order approximation of the bed pressure includes the thickness gradient, leading to non-hydrostatic pressure. In 3D models the static equilibrium condition depends on the derivative of the pressure in the direction normal to the topography and not only on the bed pressure, as in depth-averaged shallow models. In this paper we show that the static equilibrium criteria deduced for the 3D model proposed in [15] coincides with one of the depth-averaged models when including the proposed correction of the friction term.

After presenting the model and coordinate system for granular flows over a 1D topography in section 2, we explain the limitation of shallow flow models in terms of their capacity to handle the threshold of motion and propose a new direction to modify the motion criterion (section 3). This is done in two subsections. The first deduces the definition of the friction term from the preservation of the stationary solutions of the model. The second shows that this correction implies that the static equilibrium condition coincides with the criteria of the 3D model introduced in [15], where a second order correction of the pressure is considered. Then, in section 4, we extend the model and the modification of the motion criterion to granular flows on 2D topography. Firstly the general case is presented, where the computed thickness of the granular flow is perpendicular to the bottom and curvature terms are considered. Secondly, a particular case, defined in terms of a reference plane, is presented. This section finishes with a proof that (1) the 1D models exactly preserve the physical solutions at rest defined by the repose angle of the material, and (2) the 2D models preserve them up to second order in terms of ε, the ratio between the characteristic thickness and along-slope length of the granular flow. Finally, in section 5 we show numerical results highlighting the problems related to the threshold of motion and how the modified criterion affects the simulations. The results and the limitation of the proposed modification are discussed on the basis of comparison with 2D and 3D laboratory experiments.

2 Model equations and coordinate system

For clarity we first focus on the 1D case. Cartesian coordinates are denoted by $\vec{x} = (x, z)$. As in classical models, we consider a granular mass over an inclined plane of slope θ. The reference plane is then determined by a fixed point $(\bar{x}, \bar{z})$ and its slope $\tan\theta$ (Figure 1(b)). As in our previous work [17], for every point M in the grain layer, we introduce the coordinates $\vec{X} = (X, Z)$, X being the abscissa of the orthogonal projection of M onto the reference plane and Z being the distance from M to the

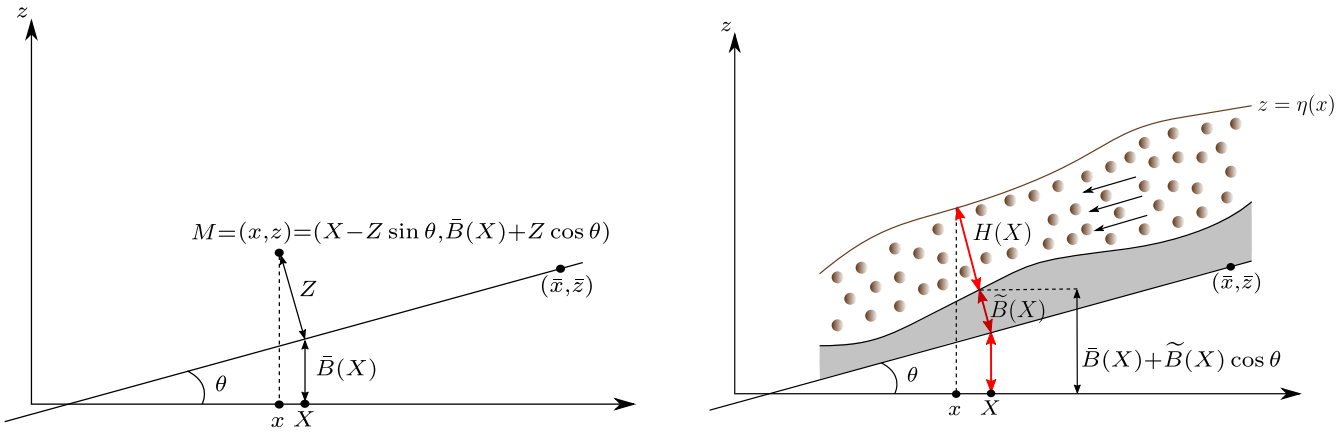

(a) Coordinate systems

(b) Notation for the topography and the granular layer at time t

Figure 1: Coordinates and notation of the system

reference plane (see Figure 1(a)). The relation between Cartesian coordinates $\vec{x}$ and $\vec{X}$ coordinates is

$$\vec{x} = (X - Z\,\sin\theta, \bar{B}(X) + Z\cos\theta), \tag{5}$$

where $\bar{B}(X)$ is the level of the reference plane:

$$\bar{B}(X) = \bar{z} + \tan\theta(X - \bar{x}). \tag{6}$$

The fixed topography is defined by $\widetilde{B}(X)$ as the distance, with sign, of the bottom level to the reference plane. Note that $\bar{B}(X) + \widetilde{B}(X)\cos\theta$ designates the vertical distance (with sign) from the bottom to the abscissa axis.

As already mentioned, we focus on the depth-averaged shallow model developed to describe granular flows. We use here the Savage-Hutter model [1] as the base model for our case study by assuming isotropy of normal stresses ($\sigma_{xx} = \sigma_{zz}$).

This model can be written in $\vec{X}$ coordinates in the following form:

$$\begin{cases} \partial_t H + \cos\theta\ \partial_X(HU) = 0, \\ \\ \partial_t(HU) + \cos\theta\partial_X(HU^2) = -gH\cos\theta\Big(\partial_X\bar{B} + \partial_X(\widetilde{B} + H)\ \cos\theta\Big) - P_b\,\mu_b\,\mathrm{sgn}(U), \end{cases} \tag{7}$$

where $H = H(X,t)$ denotes the thickness of the granular mass perpendicular to the reference plane, $U = U(X,t)$ the velocity component parallel to the reference plane and μ_b the basal friction coefficient given by one of the laws (4) or (3), already presented and

$$P_b = \frac{p_b}{\rho},$$

where p_b is the bed pressure (i.e. normal stress) involved in the friction term. In most models, the pressure is assumed to be hydrostatic. Let us denote the hydrostatic bed pressure as $P_{bh} = p_{bh}/\rho$, then

$$P_b = P_{bh} = gH\cos\theta.$$

Inertial forces are on the left hand side of the momentum equation while the right hand side corresponds to the force of gravity parallel to the plane (first term), the hydrostatic pressure force linked to the thickness gradient (second term), and finally the friction force.

Remark 1. *Note that the local coordinates of a point M are given by $(X/\cos\theta, Z)$ when using the above notation. By denoting $\hat{X} = X/\cos\theta$ and taking into account that $\partial_X \bar{B} = \tan\theta$, the Savage-Hutter system is written in its original local coordinates as follows:*

$$\begin{cases} \partial_t H + \partial_{\hat{X}}(HU) = 0, \\ \\ \partial_t(HU) + \partial_{\hat{X}}(HU^2) = -gH\cos\theta\Big(\tan\theta + \partial_{\hat{X}}(\widetilde{B}+H)\Big) - P_b\,\mu_b\,\mathrm{sgn}(U). \end{cases} \tag{8}$$

For the sake of comparison with the model proposed in [1, 18], note that θ is measured with the opposite sign.

3 Reasons for the friction correction

In depth-averaged models, the interaction between the granular material and the bottom surface is determined by the basal friction force. The corresponding stress appears in the momentum equation as a term depending on a basal friction coefficient μ_b multiplied by the normal stress $gH\cos\theta$ (see last term in the momentum equation in system (7) or (8)). This term not only defines the friction effect during the flow but it is responsible of an essential task intrinsic to this problem which is to provide a threshold of motion for the Coulomb criterion. To better explain this effect and the related proposed correction, we first consider the simplest case of a constant basal friction coefficient given by equation (4): $\mu_b = \tan\delta_0$. In this case, the hysteresis is not described since $\mu_{start} = \mu_{stop} = \mu_b$.

The natural threshold of motion for a material initially at rest is given by the repose angle θ_{start} which is here equal to δ_0. This angle is measured experimentally and corresponds to the limit slope of the free surface of a pile of the granular material at rest. As a result the material stays at rest when:

$$|\partial_x \eta(x)| \leq \tan\delta_0, \tag{9}$$

where $\eta(x)$ denotes the free surface.

Let us now look at the momentum equation of system (7)

$$\partial_t(HU) + \cos\theta\,\partial_X(HU^2) + gH\cos\theta\partial_X\big(\bar{B} + (\widetilde{B}+H)\,\cos\theta\big) = -P_b\,\mu_b\,\mathrm{sgn}(U). \tag{10}$$

The solution of the model stays at rest when

$$gH\cos\theta|\partial_X\big(\bar{B} + (\widetilde{B}+H)\,\cos\theta\big)| \leq |P_b|\,\mu_b. \tag{11}$$

Taking into account that $P_b = P_{bh} = gH\cos\theta$, the condition reduces to

$$|\partial_X\big(\bar{B} + (\widetilde{B} + H)\,\cos\theta\big)| \leq \mu_b.$$

Note that $\bar{B}(X) + (\tilde{B}(X) + H(X))\,\cos\theta$ defines the free surface level $\eta(x(X))$ (hereafter called $\eta(x)$) in Cartesian coordinates (see Figure 1). So when $|\partial_X(\eta(x))| > \mu_b$, the mass should flow and it should not move when (11) is fulfilled. The same condition (11) is found for the local coordinates because $\partial_{\hat{X}}(\widetilde{B} + H) = \cos\theta\ \partial_X(\widetilde{B} + H)$ (see Remark 1). The threshold criteria (11) should correspond to the physical criteria (9). This directly implies the equality $|\partial_X(\eta(x))| = |\partial_x(\eta(x))|$. This is however not true for any definition of the $\vec{X}$ coordinates (equivalently, local coordinates). Let us illustrate this with the following basic example. Figure 2 shows a granular avalanche flowing over an inclined plane. Consider two points X_1 and X_2 on the abscissa axis, and the two corresponding points $x_i = X_i - \big(\widetilde{B}(X_i) + H(X_i)\big)\sin\theta$, $i = 1, 2$. If we look at the position of the free surface measured in the vertical direction we see that

$$\eta(x_i) = \bar{B}(X_i) + \big(\widetilde{B}(X_i) + H(X_i)\big)\cos\theta.$$

As $X_2 - X_1 \neq x_2 - x_1$, the slope of the blue line (local) is different from the slope of the red line (cartesian),

$$\frac{\Big(\bar{B}(X_2) + (\widetilde{B}(X_2) + H(X_2))\ \cos\theta\Big) - \Big(\bar{B}(X_1) + (\widetilde{B}(X_1) + H)(X_1))\ \cos\theta\Big)}{X_2 - X_1} \neq \frac{\eta(x_2) - \eta(x_1)}{x_2 - x_1}.$$

Hence, in general $|\partial_X\big(B + (\widetilde{B} + H)\,\cos\theta\big)| \neq |\partial_x\eta(x)|$, except for uniform flows for which $\widetilde{B} + H$ is constant. This means that the criterion of motion provided by the mathematical model (11) provides an erroneous threshold of motion. In order to get the right free surface gradient to compare to the avalanche or repose angle, the criterion (11) must be modified and this is what we propose to focus on below.

At the free surface, the relation between Cartesian and $\vec{X}$ coordinates is given by $x = X - \big(\widetilde{B}(X) + H(X)\big)\sin\theta$, so we have

$$\partial_X(\eta(x)) = \partial_X\big(\bar{B}(X) + \big(\widetilde{B}(X) + H(X)\big)\ \cos\theta\big) = \mathcal{J}\,\partial_x(\eta(x)), \tag{12}$$

where $\mathcal{J} = \partial_X x = 1 - \partial_X\big(\widetilde{B}(X) + H(X)\big)\sin\theta$ is the Jacobian of the previous change of coordinates related to the $\vec{X}$ coordinates.

Keeping in mind the above connection between $\partial_X\eta$ and $\partial_x\eta$, Figure 3 shows pathological situations at the front and at the rear parts of a typical initial condition of a granular mass on an inclined plane. For simplicity, we consider $\widetilde{B} = 0$. At the front part $\mathcal{J} < 1$ (Figure 3(a)) while at the rear part $\mathcal{J} > 1$ (Figure 3(b)). In these figures, the dashed lines (respectively, dashed-dotted lines) have slope μ_b (respectively, $\partial_X\eta$). In Figure 3(a), the granular mass should move downward since $|\partial_x\eta| > \mu_b$, but the solution of the model will not experience any motion because $|\partial_X\eta| < \mu_b$. On the contrary, at the rear part (Figure 3(b)), the granular mass should stay at rest ($|\partial_x\eta| < \mu_b$), but the model solution starts flowing since $|\partial_X\eta| > \mu_b$. As a result, the stopping criteria fails when

$$(\mathcal{J} < 1 \text{ and } |\partial_X\eta| < \mu) \text{ or } (\mathcal{J} > 1 \text{ and } |\partial_X\eta| > \mu).$$

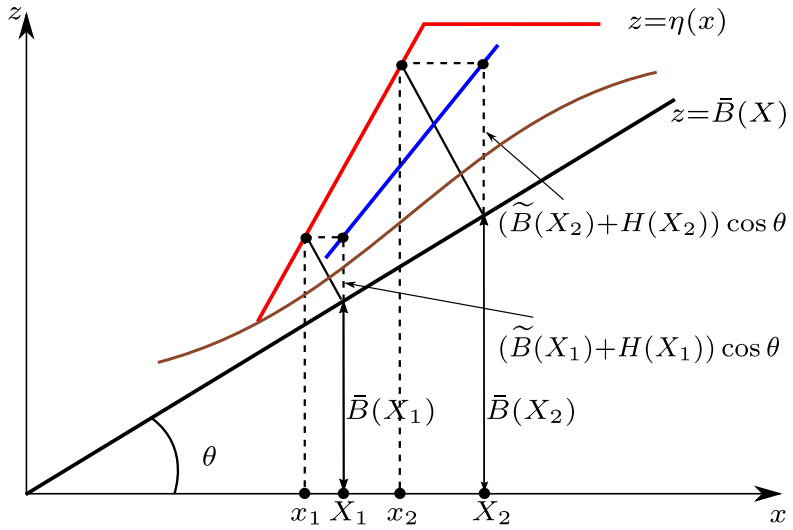

Figure 2: A basic example showing the problem with the friction coefficient

So, in order to get the right threshold of motion defined by (9) and given that $|\partial_x\eta(x)| = |\mathcal{J}^{-1}\partial_X(\eta(x))|$, we propose the following correction of the bed pressure involved in the friction term,

$$P_b = P_{b,\mathcal{J}} = \frac{p_{bh}}{\rho}|\mathcal{J}| = gH\cos\theta|\mathcal{J}|, \quad \text{with} \quad \mathcal{J} = 1 - \partial_X\big(\widetilde{B}(X) + H(X)\big)\sin\theta. \tag{13}$$

P_b should therefore be replaced by $P_{b,\mathcal{J}}$ in model (7). With this correction, the motion criterion (11) becomes

$$|\partial_X(\eta(x))| \leq |\mathcal{J}|\mu \tag{14}$$

which is equivalent to $|\partial_x\eta(x)| \leq \mu_b$ in view of (12) and (13). Note that $P_{b,\mathcal{J}} = P_{bh}$ for uniform flows.

Note that the value of the Jacobian is affected not only by the variation of H but also by the variation of $\widetilde{B}$ (the distance, with sign, between the bottom and a given reference plane). In general, to consider a reference plane is appropriate when the bottom is close to a plane defined by an averaged slope. Nevertheless, the influence of the variation of $\widetilde{B}$ in the definition of $\mathcal{J}$ could be significantly greater than the variation of H in situations where the bottom is far from the reference plane. In order to study this influence in the numerical test section, we investigate separately the H- and $\widetilde{B}$-dependence of $\mathcal{J}$ by introducing the following definition for the $\widetilde{B}$ related correction,

$$\mathcal{J}_{\widetilde{B}} = 1 - \partial_X\big(\widetilde{B}(X)\big)\sin\theta. \tag{15}$$

Remark 2. *We have illustrated the failure of depth-averaged shallow models to accurately describe the motion threshold by first considering a constant basal friction coefficient* (4) *but the same reasoning can be followed for any other definition of the friction coefficient. In the case of the more complex law proposed by Pouliquen and Forterre [3] two threshold angles are considered,* θ_{start} *and* θ_{stop}*. In any case, these angles are always measured from the horizontal and compared to the free surface gradient.*

We have illustrated here the imprecision of the threshold motion criterion in depth-averaged models and exposed the main reasoning leading to their correction, based on simple geometrical considerations.

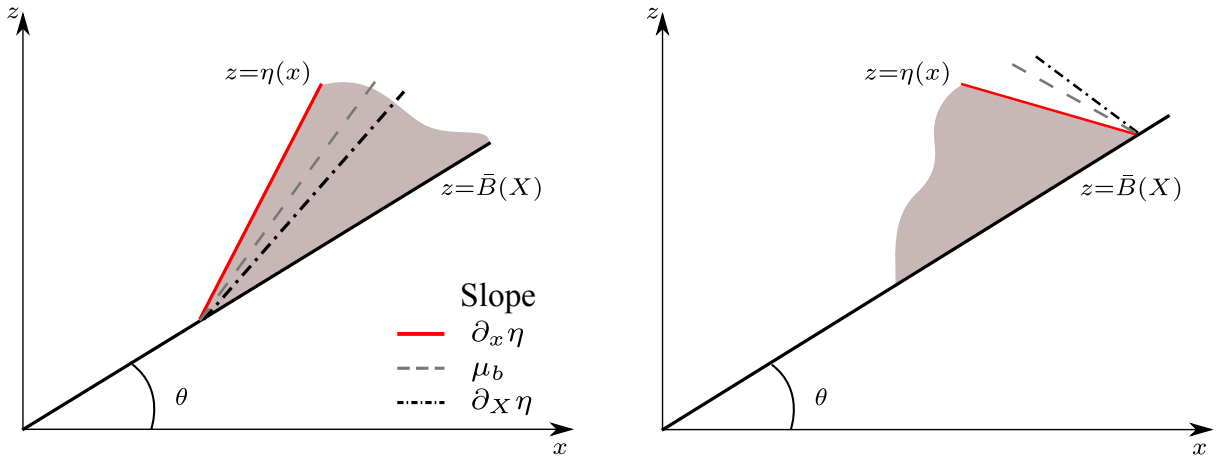

(a) $\mathcal{J} < 1$ (b) $\mathcal{J} > 1$

Figure 3: Pathological situations in the model without correction. Dashed lines have slope μ_b and dashed-dotted lines have slope $\partial_X \eta$. Left: a zoom of the front part of the granular avalanche ($\mathcal{J} < 1$); since $|\partial_X \eta| < \mu_b < |\partial_x \eta|$, the avalanche should start flowing but the solution of the model will not. Right: a zoom of the rear part ($\mathcal{J} > 1$): then $|\partial_x \eta| < \mu_b < |\partial_x \eta|$, so the avalanche should stay at rest but the solution will move upward.

In the following, we give a more formal derivation of this correction (subsection 3.1) and a possible interpretation of its origin (subsection 3.2).

3.1 Formal model deduction of the correction in the friction term

We will now provide a formal deduction of the correction proposed above (13) based on a depth-averaging process including a change of coordinates. For the sake of simplicity, the 1D case is presented. The general correction for 2D models is presented in section 4.

The last term of the right hand side of the momentum equation in system (7) corresponds to the bed shear stress of the avalanche τ_b obtained after a Z-integration process and considering the Coulomb boundary condition at the bottom. We consider the system (7) as the starting point in the following manner:

$$\begin{cases} \partial_t H + \cos\theta \partial_X (HU) = 0, \\ \partial_t (HU) + \cos\theta \partial_X (HU^2) = -gH \cos\theta \, \partial_X \big(\bar{B} + (\widetilde{B} + H) \cos\theta \big) - \dfrac{\tau_b}{\rho}, \end{cases} \tag{16}$$

ρ being the density of the granular material and τ_b the friction term at the bottom to be defined. The idea is to find the expression of the friction term τ_b that would lead to the correct threshold of motion (9).

To write the above equations in Cartesian coordinates, we introduce the change of coordinates

$$(x, t) \mapsto (X, t)$$

where, for each (x,t), $X = X(x,t)$ is implicitly determined by the equality

$$x = X(x,t) - \Big(\widetilde{B}\big(X(x,t)\big) + H\big(X(x,t),t\big)\Big)\sin\theta. \tag{17}$$

We use the following notation

$$h(x,t) = H\big(X(x,t),t\big), \quad u(x,t) = U\big(X(x,t),t\big),$$

$$\bar{b}(x,t) = \bar{B}\big(X(x,t)\big) \quad \text{and} \quad \tilde{b}(x,t) = \widetilde{B}\big(X(x,t)\big).$$

Then the Jacobian matrix is

$$A := \nabla_{(x,t)}(X,t) = \begin{pmatrix} 1 + \partial_x(\tilde{b}+h)\,\sin\theta & \partial_t(\tilde{b}+h)\,\sin\theta \\ 0 & 1 \end{pmatrix}$$

and the Jacobian of the change of coordinates is

$$\widehat{\mathcal{J}} := \det(\nabla_{(x,t)}(X,t)) = 1 + \partial_x(\tilde{b}+h)\,\sin\theta.$$

Hence $\mathcal{J} = \det(\nabla_{(X,t)}(x,t)) = \widehat{\mathcal{J}}^{-1}$.
We apply this change to each equation of system (16) by using the divergence chain rule (see [19, Lemma 2.1]), $\nabla_{(X,t)} \cdot \vec{f} = \dfrac{1}{\widehat{\mathcal{J}}}\nabla_{(x,t)} \cdot (\widehat{\mathcal{J}} A^{-1}\vec{f})$ for any vector $\vec{f}$. This leads to

$$\begin{cases} \partial_t(h\widehat{\mathcal{J}}) + \partial_x(h\,u_c) = 0, \\ \partial_t(hu\widehat{\mathcal{J}}) + \partial_x(hu\,u_c) = -gh\cos\theta\,\Big(\partial_x\big(\bar{b} + (\tilde{b}+h)\,\cos\theta\big) + \dfrac{1}{gh\cos\theta}\dfrac{\tau_b}{\rho}\widehat{\mathcal{J}}\Big) \end{cases} \tag{18}$$

where

$$u_c = \cos\theta\, u - \partial_t(\tilde{b}+h)\sin\theta.$$

Note that $\bar{b} + (\tilde{b}+h)\,\cos\theta = \eta(x)$. Then, when the material is at rest, the balance of forces on the right hand side member of the momentum equation in (18) gives:

$$|\partial_x(\eta(x))| = \Big|\frac{1}{\rho g h\cos\theta}\,\tau_b\widehat{\mathcal{J}}\Big|. \tag{19}$$

In order to obtain $|\partial_x\eta(x)| = \mu_b$ as the threshold of motion, it is necessary to define τ_b such that

$$\frac{1}{\rho g h\cos\theta}\,\tau_b\,|\widehat{\mathcal{J}}| = \operatorname{sgn}(u)\mu_b$$

(the absolute value is taken to ensure that the friction force acts opposite to the velocity, so its sign must be determined by the sign of the velocity). Thus, considering that $\widehat{\mathcal{J}} = \mathcal{J}^{-1}$ and returning to the previous notation, we have

$$\frac{\tau_b}{\rho} = gH\cos\theta|\mathcal{J}|\operatorname{sgn}(U)\mu_b\ . \tag{20}$$

Then the corrected model becomes

$$\begin{cases} \partial_t H + \cos\theta \partial_X (HU) = 0, \\ \partial_t (HU) + \cos\theta\, \partial_X (HU^2) + gH\cos\theta \partial_X \big(\bar{B} + (\widetilde{B} + H)\, \cos\theta\big) = -P_{b,\mathcal{J}}\, \mu_b\, \mathrm{sgn}(U). \end{cases} \tag{21}$$

where $P_{b,\mathcal{J}}$ is defined in equation (13).

Nevertheless, note that the reasoning developed above is only true for the initiation of motion, that is, for a granular mass initially at rest. Hence, once the avalanche is flowing, the balance of forces to obtain the Coulomb criterion also involves the inertial forces [4]. So, additional terms would have to be considered and their orders of magnitude may be significant. As a result, the validity of the modification of the bed pressure defining the friction term (13) proposed above may not be valid during the flow. Taking into account the correction (13) in the momentum equations during the flowing phase, may lead to an error of the order of $H \sin\theta \mu_b \partial_X \big(\widetilde{B} + H\big)$, since $P_{b,\mathcal{J}} \mu_b = gH\cos\theta |1 - \partial_X \big(\widetilde{B} + H\big) \sin\theta| \mu_b$ in the evolution phase. However, for nearly uniform flows, this term will be close to zero. The effect of the correction during the flow will be analyzed in the numerical tests.

3.2 Static equilibrium condition and second order correction of the pressure

In this subsection we investigate another possible reason for the proposed correction. For simplicity we consider $\tilde{B} = 0$.

The Coulomb criterion is usually written in terms of the tangential and normal stresses at the bed, the latter being multiplied by the friction coefficient. Thus for a depth-averaged model

$$|\tau_b| \leq \mu_b\ |(\sigma_n)_{|b}| = \mu_b |p_b|. \tag{22}$$

If we consider the hydrostatic pressure, then $p_b = p_{bh} = \rho P_{bh} = \rho g H \cos\theta$, giving the friction term appearing on the right hand side of the momentum equation in models (7) and (8),

$$\mu_b P_{bh} = \mu_b\ \mathrm{sgn}(U)\ gH\cos\theta.$$

In this way, the modification (13) can be seen as a correction of the pressure value at the bottom,

$$P^*_{|b} = gH\cos\theta\ |\mathcal{J}| = gH\cos\theta |1 - \sin\theta\ \partial_X H|. \tag{23}$$

Note that the additional term depends on the variation of the height ($g\cos\theta\sin\theta\ H\partial_X H$) and it is of the order of ε^2 (ε denoting the classical parameter measuring the shallow flow assumption, considering asymptotically that $H \sim \varepsilon$). This leads us to look for a more accurate approximation of the pressure, namely to the third order in ε.

In [15] the authors introduce a model to describe the evolution of the static/flowing interface, denoted here by $Z = \tilde{b}(t, X)$, in a viscoplastic flow with Drucker-Prager rheology. A third order approximation of the pressure is needed to obtain a closed system. An interesting particular model is developed for the slow flow case, assuming a small downslope velocity ($U \sim \varepsilon$) and a no-slip condition at the static/flowing interface. The following non-hydrostatic pressure value is deduced up to the third order in the flowing region (remember that $\tilde{B} = 0$),

$$P(X,Z,t) = \frac{p(X,Z,t)}{\rho}$$
$$= \varepsilon\ g\cos\theta(H-Z) + \varepsilon^2 g\cos\theta\Big(\sin\theta\partial_X H + 2\mu\,\mathrm{sgn}(\partial_Z U)\cos\theta\partial_X\tilde{b}\Big)(H-Z) + \mathcal{O}(\varepsilon^3),\ \text{for } \tilde{b} < Z < H. \tag{24}$$

The first term gives the hydrostatic approximation, the second term comes from the normal momentum contribution to the σ_{xz} component of the stress and the last term comes from the rheology law in the σ_{zz} component. In the derived approximation at the leading order, it is found that $\mu\mathrm{sgn}(\partial_Z U) = -\tan\theta + \mathcal{O}(\varepsilon)$. We thus obtain

$$P(X,Z,t) = \varepsilon\ g\cos\theta(H-Z) + \varepsilon^2 g\cos\theta\Big(\sin\theta\partial_X H - 2\sin\theta\partial_X\tilde{b}\Big)(H-Z) + \mathcal{O}(\varepsilon^3), \qquad \text{for } \tilde{b} < Z < H. \tag{25}$$

The velocity equation of the deduced 2D model reads

$$\partial_t U + g(\sin\theta + \cos\theta\partial_X(H\cos\theta)) + \mathrm{sgn}(\theta)\partial_Z(\mu p) = \mathcal{O}(\varepsilon^2) \quad \text{for } \tilde{b} < Z < H.$$

The model has to be completed with the static equilibrium condition

$$g|\sin\theta + \cos\theta\partial_X(H\cos\theta)| \leq -(\partial_Z(\mu P))|_{Z=\tilde{b}}, \tag{26}$$

stating that the static region remains static. Using (25) in the case of constant μ, we obtain in dimensional variables

$$-\partial_Z(\mu P) = \mu g\cos\theta\Big(1 + \sin\theta\partial_X H - 2\sin\theta\partial_X\tilde{b}\Big) \qquad \text{for } \tilde{b} < Z < H. \tag{27}$$

When the velocity tends to zero (full arrest of the flow), the static/flowing interface tends to the free surface, that is $\tilde{b} = H$. As a consequence, from (26) and (27) the static equilibrium condition reads

$$|\sin\theta + \cos\theta\partial_X(H\cos\theta)| \leq \mu\cos\theta(1 - \sin\theta\partial_X H).$$

Since the free surface is $\eta = \bar{B} + H\cos\theta$, this is equivalent to

$$|\partial_X\eta| \leq \mu(1 - \sin\theta\partial_X H).$$

As μ is assumed to be constant, we have $\mu = \mu_b$, thus this static equilibrium condition coincides with (14). That is, the proposed friction correction for depth-averaged models will give the same equilibrium condition as in the model introduced in [15], that is associated with the pressure expansion (25). Nevertheless, we can not recover this additional term directly from non-hydrostatic depth-averaged models such as the one in [20].

Furthermore, in [21, 22] the authors present an accurate approximation of the pressure at the bottom at the third order in ε where no rheology is considered and for a non-slow flow ($U = \mathcal{O}(1)$). The additional terms to the hydrostatic pressure at the bottom involve the velocity and read as

$$P_{|b} = \varepsilon\ gH\cos\theta - \varepsilon^2\ \cos\theta\ \partial_t\Big(\frac{H^2}{2}\partial_X U\Big) - \varepsilon^2\ (\cos\theta)^2\ \partial_X\Big(\frac{H^2}{2}U\partial_X U\Big) + \mathcal{O}(\varepsilon^3),$$

or in the original local coordinates $\hat{X} = \frac{X}{\cos\theta}$,

$$P_{|b} = \varepsilon\ gH\cos\theta - \varepsilon^2\ \partial_t\Big(\frac{H^2}{2}\partial_{\hat{X}}U\Big) - \varepsilon^2\ \partial_{\hat{X}}\Big(\frac{H^2}{2}U\partial_{\hat{X}}U\Big) + \mathcal{O}(\varepsilon^3).$$

Note that the correction terms vanish for $U = 0$ and become of order ε^3 under the previous slow flow assumption ($U \sim \varepsilon$). Nevertheless they become significant during the evolution phase when the velocity is not small, and they are of the same order ε^2 as the previous correction in (24).

The above discussion reinforces the idea already presented that the proposed modification to the friction coefficient (23) (hence (13)) could be meaningful only when the flow is close to stopping or exactly static, and we have no guarantee for its correctness otherwise. In the numerical tests we will assess the influence of the Jacobian correction during the flow evolution, and show that its effect is more noticeable at the starting and stopping phases.

4 Proposed 2D model with friction correction

In this section we introduce a correction of the 2D model introduced by Bouchut and Westdickenberg in [16] for general topographies. $B(X, Y)$ denotes the scalar function defining the topography and X, Y the horizontal coordinates (see Figure 4).

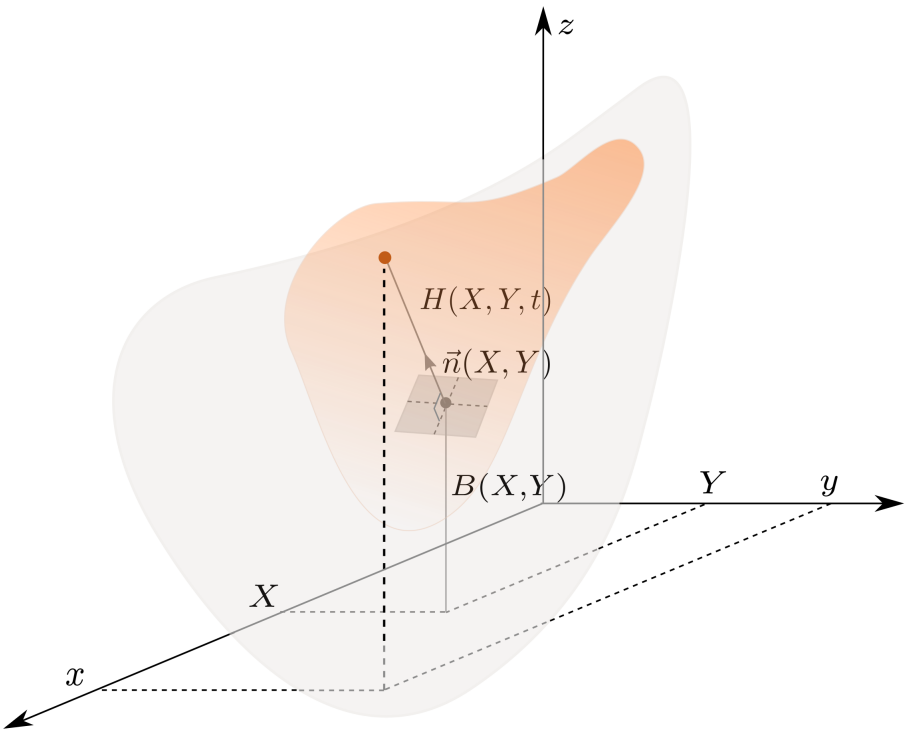

Figure 4: Domain and notation. The general 2D topography is represented in gray and the granular mass in brown.

The normal to the topography at each point is calculated through a 3-D unit upward normal vector

$$\vec{n} = (\frac{-\boldsymbol{\nabla_X} B}{\sqrt{1+||\boldsymbol{\nabla_X} B||^2}}, \frac{1}{\sqrt{1+||\boldsymbol{\nabla_X} B||^2}}) = (-\boldsymbol{s}, c) \in \mathbb{R}^2 \times \mathbb{R} \tag{28}$$

where $\boldsymbol{X} = (X, Y) \in \mathbb{R}^2$ and, the scalar $c = \cos\theta$ is the cosine of the angle between the vertical direction and the normal $\vec{n}$. In our notation, the 3-D vectors are denoted by $\vec{.}$, whereas the 2-D vectors are written in bold. The flow is described by

$$H(\boldsymbol{X}, t) \geq 0, \quad \boldsymbol{U'}(\boldsymbol{X}, t) \in \mathbb{R}^2 \tag{29}$$

where H is the thickness of the avalanche in the direction normal to the topography. Then, the free surface position is defined by (see Figure 4),

$$(x, y, \eta(x, y)) = (X, Y, B(X, Y)) + H(X, Y, t)\ \vec{n}(X, Y). \tag{30}$$

The velocity vector $\boldsymbol{U'} = (U', V')$ is a parametrization of the velocity. This parametrization has been defined to simplify the equations with topography. The real 3-D material velocity has horizontal/vertical components defined by

$$\vec{U} = (\, c\boldsymbol{U'}\,,\ \boldsymbol{s}\cdot\boldsymbol{U'}\,). \tag{31}$$

This physical velocity is tangent to the topography, that is, $\vec{U}\cdot\vec{n} = 0$, as would be expected for shallow flows. In the horizontal Cartesian coordinate formulation, the model can be expressed as

$$\begin{cases} \partial_t(H/c) + \boldsymbol{\nabla_X}\cdot(H\boldsymbol{U'}) = 0, \\ \\ \partial_t\boldsymbol{U'} + c\,\boldsymbol{U'}\cdot\boldsymbol{\nabla_X}\boldsymbol{U'} + \dfrac{1}{c}(\mathcal{I} - \boldsymbol{s}\boldsymbol{s^t})\boldsymbol{\nabla_X}(g(H\,c + B)) = \dfrac{-1}{c}(\boldsymbol{U'^t}\,\mathcal{H}\,\boldsymbol{U'})\,s + \dfrac{1}{c}(\boldsymbol{s^t}\mathcal{H}\boldsymbol{U'})\boldsymbol{U'} \\ \qquad\qquad\qquad\qquad\qquad\qquad\qquad\qquad\qquad\qquad\qquad\qquad - \dfrac{P_{b,\mathcal{J}}\mu_b\,\boldsymbol{U'}}{H\sqrt{c^2\,\|\boldsymbol{U'}\|^2 + (\boldsymbol{s}\cdot\boldsymbol{U'})^2}}(1 + \dfrac{\boldsymbol{U'^t}\,\mathcal{H}\,\boldsymbol{U'}}{gc})_+ \end{cases} \tag{32}$$

where

$$P_{b,\mathcal{J}} = gHc\,|1 - \mathbf{s}\cdot\boldsymbol{\nabla_X} H|,$$

$\boldsymbol{\nabla_X}$ is the gradient vector in the horizontal (X, Y) plane, g is the acceleration due to gravity and $\mathcal{I}$ is the identity matrix. The subscript + stands for the positive part, $a_+ = max(0, a)$ (see [16] and [5] for more details). In this model the curvature tensor of the topography is taken into account, expressed as

$$\mathcal{H} = c^3 \begin{pmatrix} \dfrac{\partial^2 B}{\partial X^2} & \dfrac{\partial^2 B}{\partial X \partial Y} \\ \\ \dfrac{\partial^2 B}{\partial X \partial Y} & \dfrac{\partial^2 B}{\partial Y^2} \end{pmatrix}. \tag{33}$$

Note that model (32) differs from the one introduced in [16] in the term $P_{b,\mathcal{J}}$, by the factor $|1 - \mathbf{s}\cdot\boldsymbol{\nabla_X} H|$.

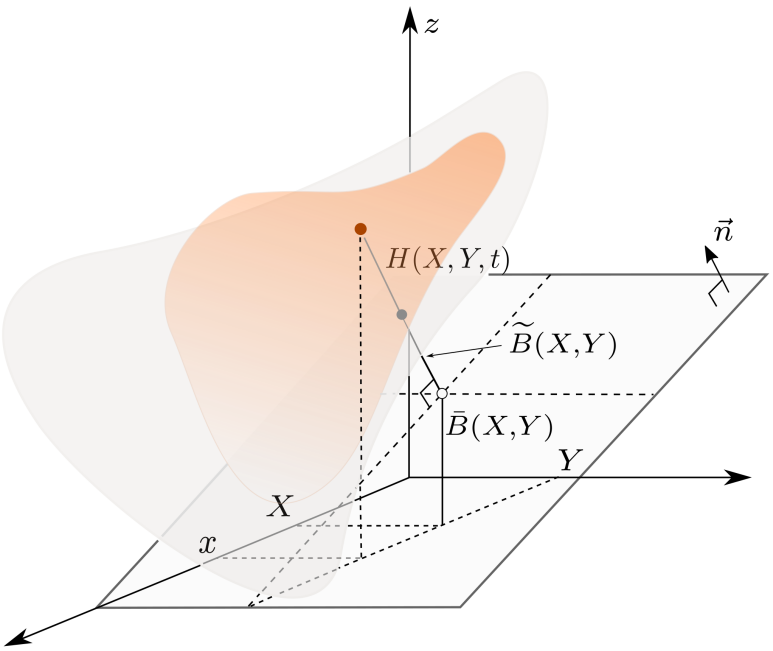

Figure 5: Domain and notation. Definition of the topography represented in yellow with respect to a reference plane represented in gray. The granular mass is shown in orange.

4.1 Model with a reference plane

We will also consider a simplification of this model, where the topography is defined with respect to a reference plane, defined by

$$\bar{B}(X,Y) = \bar{z} + \tan\theta(X - \bar{x}). \tag{34}$$

The vector normal to the reference plane is

$$\vec{n} = (-\sin\theta\,, 0\,, \cos\theta\,) \tag{35}$$

We will also denote by $\widetilde{B}(X,Y)$ the distance, with sign, of the bottom level to the reference plane. Finally, $H(X,Y,t)$ is the thickness of the avalanche in the direction normal to the reference plane. Then, the free surface position is defined by

$$(x,y,\eta(x,y,t)) = (X,Y,\bar{B}(X,Y)) + H(X,Y,t)(-\sin\theta, 0, \cos\theta).$$

Note that in this case $y = Y$. The model can then be deduced as a particular case of (37), by considering

$$B(X,Y) = \bar{B}(X,Y) + \cos\theta\,\tilde{B}(X,Y),$$

$$\boldsymbol{s} = (\sin\theta,\, 0\,), \quad c = \cos\theta \quad \text{and} \quad \mathcal{H} = 0.$$

We then have that the following definition of velocity vector $\boldsymbol{U'}$,

$$\boldsymbol{U'} = (U, V/\cos\theta),$$

where the velocity component parallel to the Y-axis is V and the 3D material velocity, tangent to the reference plane, is

$$\vec{U} = (\cos\theta\, U\,,\, V\,,\, \sin\theta\, U). \tag{36}$$

The model including the bed pressure correction in the friction term can then be written as follows:

$$\begin{cases} \partial_t(H) + \boldsymbol{\nabla_X} \cdot (H\, \cos\theta\, \boldsymbol{U'}) = 0, \\ \\ \partial_t \boldsymbol{U'} + \cos\theta\, \boldsymbol{U'} \cdot \boldsymbol{\nabla_X} \boldsymbol{U'} + g\cos\theta\, \boldsymbol{\nabla_X}(\bar{B} + \cos\theta\,(\tilde{B} + H)) = -\dfrac{P_{b,\mathcal{J}}\mu_b\, \boldsymbol{U'}}{H\sqrt{U^2+V^2}}, \end{cases} \tag{37}$$

where

$$P_{b,\mathcal{J}} = gH\cos\theta\,|1 - \sin\theta\,\partial_X(\tilde{B} + H)|.$$

Note that for 1D flows, where $V = 0$, $\partial_Y H = 0$ and $\partial_Y \tilde{B} = 0$, this system reduces to the 1D model proposed in section 3, defined by equation (21).

4.2 Well-balanced property of the models

In this section we present the proof of the property of the proposed models: to preserve the material at rest solution when the slope of the free surface is smaller than the tangent of the repose angle. As described above, this property is not verified by classical depth-averaged models such as Savage-Hutter models.

We consider the change of coordinates

$$\boldsymbol{x} = \boldsymbol{X} - \mathbf{s}\, H(\boldsymbol{X}, t), \tag{38}$$

and the notation

$$h(\boldsymbol{x}, t) = H\big(\boldsymbol{X}(\boldsymbol{x}, t), t\big), \quad b(\boldsymbol{x}, t) = B\big(\boldsymbol{X}(\boldsymbol{x}, t)\big). \tag{39}$$

Then, according to (30) the free surface is defined by

$$\eta(\boldsymbol{x}, t) = h(\boldsymbol{x}, t)\, c + b(\boldsymbol{x}).$$

THEOREM **1.** *The models defined either by system (32) or by system (37) preserve the steady solution of material at rest when the maximum angle of the free surface, measured from the horizontal, is smaller than the repose angle of the material, that is*

$$\|\boldsymbol{\nabla_x}(h\, c + b)\| \leq \mu, \tag{40}$$

up to second order ($\mathcal{O}(\epsilon^2)$) for 2D shallow flows where $H = \mathcal{O}(\epsilon)$, ϵ being a small value. Moreover, it is exactly preserved for 1D flows.

PROOF

For the sake of brevity we present the proof only for the system (32). The proof for system (37) is analogous. The exact preservation of steady solutions at rest in 1D can be deduced from the reasoning in Subsection 3.1.

The solution to the system (32) is at rest if $\boldsymbol{U'} = 0$ and

$$\left\| \frac{\mathcal{I} - \mathbf{s}\mathbf{s}^t}{c} \boldsymbol{\nabla_X}(H\,c + B) \right\|_{topo}^2 \leq \mu^2 c^2 (1 - \mathbf{s} \cdot \boldsymbol{\nabla_X} H)^2, \tag{41}$$

where for a two-dimensional vector R we set

$$\|R\|_{topo}^2 = c^2 \|R\|^2 + (s \cdot R)^2.$$

When $R = \frac{\mathcal{I} - \mathbf{s}\mathbf{s}^t}{c} G$ for some two-dimensional vector G, note that

$$\|R\|_{topo}^2 = G^t (\mathcal{I} - \mathbf{s}\mathbf{s}^t) G.$$

For (41) we have $G = \boldsymbol{\nabla_X}(H\,c + B)$, thus

$$\left\| \frac{\mathcal{I} - \mathbf{s}\mathbf{s}^t}{c} \boldsymbol{\nabla_X}(H\,c + B) \right\|_{topo}^2 = \nabla_X (H\,c + B)^t (\mathcal{I} - \mathbf{s}\mathbf{s}^t) \boldsymbol{\nabla_X}(H\,c + B).$$

We have

$$\boldsymbol{\nabla_X}(H\,c + B) = \boldsymbol{\nabla_X}(H\,c) + \frac{\mathbf{s}}{c},$$

therefore

$$\left\| \frac{\mathcal{I} - \mathbf{s}\mathbf{s}^t}{c} \boldsymbol{\nabla_X}(H\,c + B) \right\|_{topo}^2 = |\mathbf{s}|^2 + 2\,c\,\mathbf{s}^t\,\boldsymbol{\nabla_X}(H\,c) + (\boldsymbol{\nabla_X}(H\,c))^2 - \left(\mathbf{s}^t \boldsymbol{\nabla_X}(H\,c)\right)^2.$$

Since $(\boldsymbol{\nabla_X}(H\,c))^2 = \mathcal{O}(\epsilon^2)$, up to $\mathcal{O}(\epsilon^2)$ we obtain

$$\left\| \frac{\mathcal{I} - \mathbf{s}\mathbf{s}^t}{c} \boldsymbol{\nabla_X}(H\,c + B) \right\|_{topo}^2 = \|\mathbf{s} + c\,\boldsymbol{\nabla_X}(H\,c)\|^2 = c^2 \left\| \frac{\mathbf{s}}{c} + \boldsymbol{\nabla_X}(H\,c) \right\|^2 = c^2 \left\| \boldsymbol{\nabla_X}(H\,c + B) \right\|^2.$$

As a consequence, (41) is verified up to second order if

$$\|\boldsymbol{\nabla_X}(H\,c + B)\| \leq \mu |1 - \mathbf{s} \cdot \boldsymbol{\nabla_X} H|.$$

Then, with the notation introduced in (39), to obtain (40) up to a second order error from the previous inequality we have to prove that

$$\|\boldsymbol{\nabla_X}(H\,c + B)\| = \|\boldsymbol{\nabla_x}(h\,c + b)\|\,|1 - \mathbf{s} \cdot \boldsymbol{\nabla_X} H| + \mathcal{O}(\epsilon^2), \tag{42}$$

The change of coordinates (38) gives

$$\boldsymbol{\nabla_x}(h\,c + b) = \left((\mathcal{I} - \boldsymbol{\nabla_X}(\mathbf{s}\,H))^t\right)^{-1} (\boldsymbol{\nabla_X}(H\,c) + \frac{\mathbf{s}}{c}).$$

Using the approximation $(\mathcal{I}-A)^{-1}=\mathcal{I}+A+\mathcal{O}(A^2)$, we obtain

$$\left((\mathcal{I}-\boldsymbol{\nabla}_{\boldsymbol{X}}(\mathbf{s}\,H))^t\right)^{-1}=(\mathcal{I}+\boldsymbol{\nabla}_{\boldsymbol{X}}(\mathbf{s}\,H))^t+\mathcal{O}(\epsilon^2)$$

thus

$$\begin{aligned}\boldsymbol{\nabla}_{\boldsymbol{x}}(hc+b)&=(\mathcal{I}+\boldsymbol{\nabla}_{\boldsymbol{X}}(\mathbf{s}\,H))^t(\boldsymbol{\nabla}_{\boldsymbol{X}}(H\,c)+\frac{\mathbf{s}}{c})+\mathcal{O}(\epsilon^2)\\&=\frac{\mathbf{s}}{c}+\frac{1}{c}\boldsymbol{\nabla}_{\boldsymbol{X}}H+\mathcal{O}(\epsilon^2).\end{aligned}$$

Therefore

$$\|\boldsymbol{\nabla}_{\boldsymbol{x}}(h\,c+b)\|^2=\frac{|\mathbf{s}|^2}{c^2}+\frac{2s}{c^2}\cdot\boldsymbol{\nabla}_{\boldsymbol{X}}H+\mathcal{O}(\epsilon^2),$$

and

$$\|\boldsymbol{\nabla}_{\boldsymbol{x}}(hc+b)\|^2\,(1-\mathbf{s}\cdot\boldsymbol{\nabla}_{\boldsymbol{X}}H)^2=\frac{|\mathbf{s}|^2}{c^2}+2s\cdot\boldsymbol{\nabla}_{\boldsymbol{X}}H+\mathcal{O}(\epsilon^2).$$

Independently we have

$$\|\boldsymbol{\nabla}_{\boldsymbol{X}}(H\,c+B)\|^2=\frac{|\mathbf{s}|^2}{c^2}+2s\cdot\boldsymbol{\nabla}_{\boldsymbol{X}}H+\mathcal{O}(\epsilon^2).$$

Therefore we deduce that (42) holds, which concludes the proof. □

5 Numerical tests

In this section we present several numerical tests to study the influence of the proposed correction. The following notation is introduced to distinguish the models.

- RPθ refers to a model defined with respect to a *reference plane* of slope θ, where the flow thickness ($H(\boldsymbol{X},t)$) is measured perpendicularly to this plane.
- CURV refers to a model over a general 1D topography, taking into account curvature terms.
- SHALTOP corresponds to the shallow depth-averaged model specially designed to accurately describe a general 2D topography [23, 16, 24, 5, 14, 25]. Note that Shaltop coincides with CURV in the tests over a 1D topography.

The bed pressure involved in the friction term is used in all the mentioned models and can be viewed as a product

$$P_b=\mathcal{C}\,P_{bh}$$

with $P_{bh}=gH\cos\theta$, whereas the definition of $\mathcal{C}$ depends on the correction applied to the model. If no correction is used (i.e. $\mathcal{C}=1$), the corresponding solution will be referred to as NC. The correction proposed in the previous sections corresponds to $\mathcal{C}=|\mathcal{J}|=|1-\partial_X(\widetilde{B}+H)\sin\theta|$ and will be labelled as $\mathcal{J}$ (see Table 1).

As mentioned at the end of Subsection 3.1 and 3.2, the proposed modification of the bed pressure could be meaningful only for the initiation of motion and when the flow is close to the stopping phase.

Correction name	$\mathcal{C}$
NC	$\mathcal{C} = 1$
$\mathcal{J}$	$\mathcal{C} = \mathcal{J} = 1 - \partial_X(\widetilde{B} + H)\sin\theta$
$\mathcal{J}_{\widetilde{B}}$	$\mathcal{C} = \mathcal{J}_{\widetilde{B}} = 1 - \partial_X(\widetilde{B})\sin\theta$
Velocity	$\begin{cases} \mathcal{C} = \mathcal{J} & \text{if } \lvert U\rvert \leq 0.1 \cdot \lvert U\rvert_{\max} \\ \mathcal{C} = 1 & \text{otherwise} \end{cases}$
Velocity*	$\begin{cases} \mathcal{C} = \mathcal{J} & \text{if } \lvert U\rvert \leq 0.1 \cdot \lvert U\rvert_{\max} \\ \mathcal{C} = \mathcal{J}_{\widetilde{B}} & \text{otherwise} \end{cases}$
Slope	$\begin{cases} \mathcal{C} = \mathcal{J} \text{ if } (\mathcal{J} < 1 \text{ and } \lvert\partial_X\eta\rvert < \mu) \text{ or } (\mathcal{J} > 1 \text{ and } \lvert\partial_X\eta\rvert > \mu) \\ \mathcal{C} = 1 \text{ otherwise} \end{cases}$
Slope*	$\begin{cases} \mathcal{C} = \mathcal{J} \text{ if } (\mathcal{J} < 1 \text{ and } \lvert\partial_X\eta\rvert < \mu) \text{ or } (\mathcal{J} > 1 \text{ and } \lvert\partial_X\eta\rvert > \mu) \\ \mathcal{C} = \mathcal{J}_{\widetilde{B}} \text{ otherwise} \end{cases}$
Mixed	$\begin{cases} \mathcal{C} = \mathcal{J} & \text{if } \lvert U\rvert \leq 0.1 \cdot \lvert U\rvert_{\max} \text{ and} \\ & (\mathcal{J} < 1 \text{ and } \lvert\partial_X\eta\rvert < \mu) \text{ or } (\mathcal{J} > 1 \text{ and } \lvert\partial_X\eta\rvert > \mu) \\ \mathcal{C} = 1 & \text{otherwise} \end{cases}$
Mixed*	$\begin{cases} \mathcal{C} = \mathcal{J} & \text{if } \lvert U\rvert \leq 0.1 \cdot \lvert U\rvert_{\max} \text{ and} \\ & (\mathcal{J} < 1 \text{ and } \lvert\partial_X\eta\rvert < \mu) \text{ or } (\mathcal{J} > 1 \text{ and } \lvert\partial_X\eta\rvert > \mu) \\ \mathcal{C} = \mathcal{J}_{\widetilde{B}} & \text{otherwise} \end{cases}$

Table 1: Terminology of the proposed corrections. $|U|_{\max}$ denotes the maximum velocity norm of the avalanche when no correction is applied to the model.

To limit the correction to these conditions, we introduce several definitions of the correction. Table 1 summarizes the different types of corrections with the corresponding values of $\mathcal{C}$.

To finish this introduction, note that in the models with curvature effects (see equation (32)), one of the terms involving $\mathcal{H}$ results from a pressure correction involved in the friction term [25]. Accordingly, the bed pressure involved in the friction term of the model with curvature can be defined as

$$P_b = \mathcal{C}\, P_{bh} \left(1 + \frac{\boldsymbol{U'}^{\boldsymbol{t}}\, \mathcal{H}\, \boldsymbol{U'}}{gc}\right)_+ .$$

Note also that, in 1D models with curvature, $\mathcal{H}$ is only involved in the friction term and

$$P_b = \mathcal{C}\, P_{bh} \left(1 + \frac{U^2\, \mathcal{H}}{g\cos\theta}\right)_+ , \quad \text{where} \quad \mathcal{H} = \cos^3(\theta)\partial^2_{X^2} B. \tag{43}$$

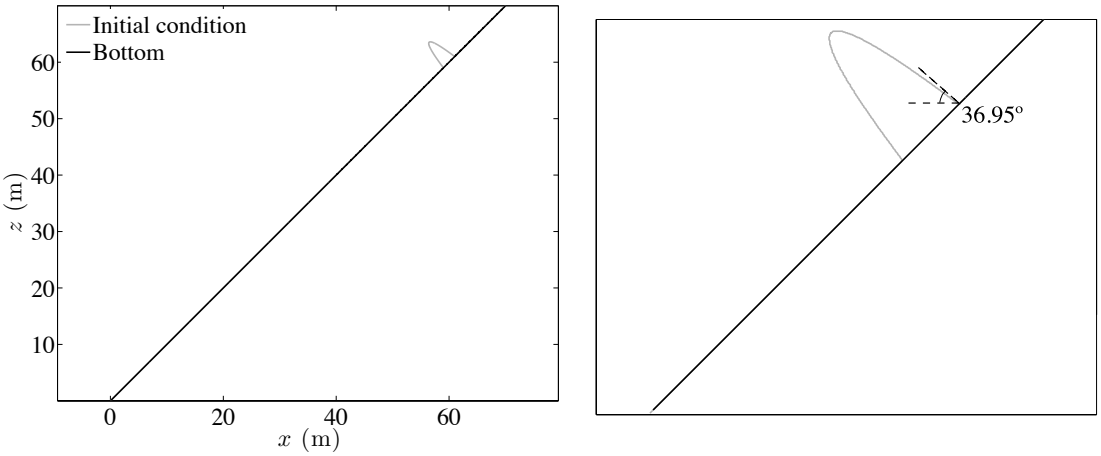

Figure 6: Test 1: Initial condition. Left: profile of the initial released mass (gray) and inclined bed (black). Right: a zoom of the profile of the initial mass.

For the SHALTOP and CURV models we will analyze the effect of the term $U^2\mathcal{H}$, by setting $\mathcal{H} = 0$ in some tests. In any case both models take into account the curvature of the topography, by the variation of θ along the domain.

5.1 Test 1: correction effects for a flow over an inclined plane

In this numerical test, we consider the spreading of a granular mass on a 45° inclined slope. The coordinate system is related to the reference slope corresponding to the sloping bed and the resulting model is called RP45. The bottom is defined as

$$\bar{B}(X) = \tan(45^\circ)X$$

and the initial condition consists in a parabolic profile given by

$$H(X) = \max\left(-5(X-59)(X-61), 0\right)$$

(see Figure 6). We consider a test over a 1D topography where the domain $X \in [0, 70]$ is discretized in 14000 cells and the CFL condition is set to 0.9.

We consider a constant friction $\mu = \tan\delta_0$ so, if the granular layer is at rest, the threshold of motion is determined by the relation between $|\partial_x\eta|$ and $\tan\delta_0$. In other words, if $|\partial_x\eta| > \tan\delta_0$ the material should flow; otherwise, if $|\partial_x\eta| \leq \tan\delta_0$, the material should not move.

Firstly, we compare the simulations obtained with the model without correction RP45-NC and the model with correction RP45-$\mathcal{J}$. Figure 7 shows the corresponding solutions at the initial instants when $\delta_0 = 30^\circ$. Differences between the two models appear in the front and the rear parts. In the rear part, the mass spreads further upslope for the model without correction (RP45-NC) than for the model with correction (RP45-$\mathcal{J}$). To investigate the origin of these differences, we have computed $|\partial_x\eta|$ at the rear part of the initial parabolic profile using (12), from which we have deduced the maximum angle of the

slope with respect to the horizontal, namely, $\arctan(|\partial_x \eta|) = 36.95^\circ$ (see Figure 6). Since $|\partial_x \eta| > \tan \delta_0$, the rear part of the mass slightly spreads upslope in both models. Nevertheless, Figure 7 clearly shows that the rear part of the avalanche simulated with the RP45-NC model spreads further upwards than the solution of the RP45-$\mathcal{J}$ model. If the same test is repeated for $\delta_0 = 37^\circ$ (no movement should occur at the rear part), Figure 8 shows that the model without correction does not satisfy the Coulomb criterion of motion whereas the model with correction $\mathcal{J}$ does.

Finally, we show the thickness H of the simulated mass corresponding to the different types of correction of the RP45 model detailed in Table 1 (see Figure 9). In these simulations we have increased the value of δ_0 up to 52° to force the avalanche to rapidly stop. The results show that the rear part of the avalanche stays at rest for all the corrected models and therefore satisfies the physical motion criterion. On the other hand, there are strong differences between the corrected models concerning the front dynamics and runout distance. The RP45-$\mathcal{J}$ model travels much further than the non-correction RP45-NC model and the models with other types of corrections (Slope, Velocity or Mixed). This means that the correction has a significant impact during the dynamics, i.e. in flow regimes where the validity of this correction can be questioned. The shape of the mass also differs slightly for the different models. The front part of the avalanches simulated with the partial corrections, i.e. where the correction is only applied in restricted conditions (Slope, Velocity or Mixed), is close to the front part simulated with the model without correction. On the other hand, the front simulated by the model with correction $\mathcal{J}$ goes significantly further.

5.2 Test 2: Dynamics and deposits for models with different corrections

In the second numerical test, we consider the spreading of a granular layer initially at rest and released on an inclined plane connected to a horizontal plane (see Figure 10).

In Cartesian coordinates, the domain is $[-15, 10]$, that we discretize in 25000 points and the CFL condition is set to 0.7. The bottom is defined as follows:

$$b(x) = \max\left(\tan(45^\circ)x, 0\right)$$

and the initial condition for the granular free surface is

$$\eta(x) = \max(\min(6.5 + 3(x - 6.5), 8.0), b(x)).$$

The simulations related to the RP models are computed with respect to the reference plane

$$z_{\text{ref}}(x) = \tan(45^\circ)x,$$

of inclination angle $\theta = 45^\circ$ (dashed line in Figure 10).

As in the previous test, a constant friction $\mu = \tan \delta_0$ is considered. Note that the maximum slope of the initial free surface is $|\partial_x \eta| = 3$. Then, if $\delta_0 \geq \arctan(3) \simeq 71.5^\circ$ the material should stay at rest, while it should move if $\delta_0 < \arctan(3)$. The objectives of this test are:

i) To check if the models ensure that the material is at rest for $\delta_0 \geq \arctan(3)$ and that the material flows if δ_0 is slightly smaller than $\arctan(3)$.

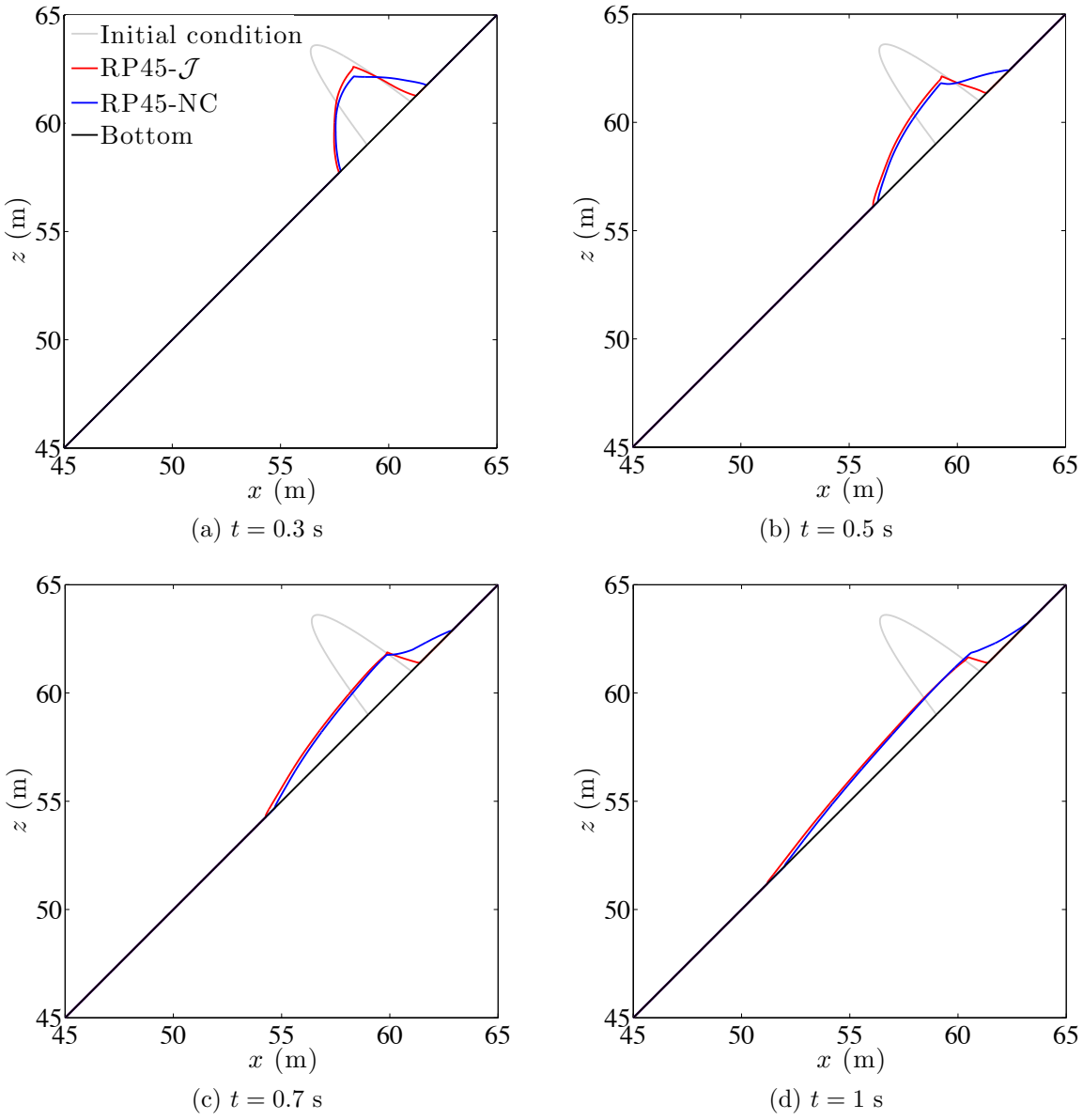

(a) $t = 0.3$ s (b) $t = 0.5$ s

(c) $t = 0.7$ s (d) $t = 1$ s

Figure 7: Test 1: Comparison between the RP45-NC and RP45-$\mathcal{J}$ models ($\delta_0 = 30°$).

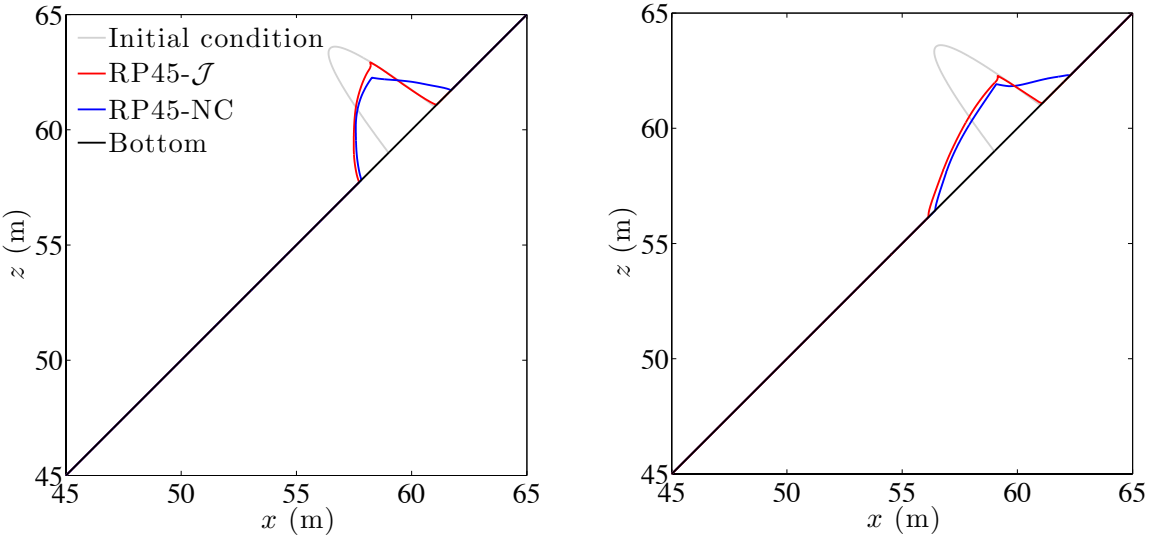

(a) $t = 0.3$ s (b) $t = 0.5$ s

(c) $t = 0.7$ s (d) $t = 1$ s

Figure 8: Test 1: Comparison between the RP45-NC and RP45-$\mathcal{J}$ models ($\delta_0 = 37°$).

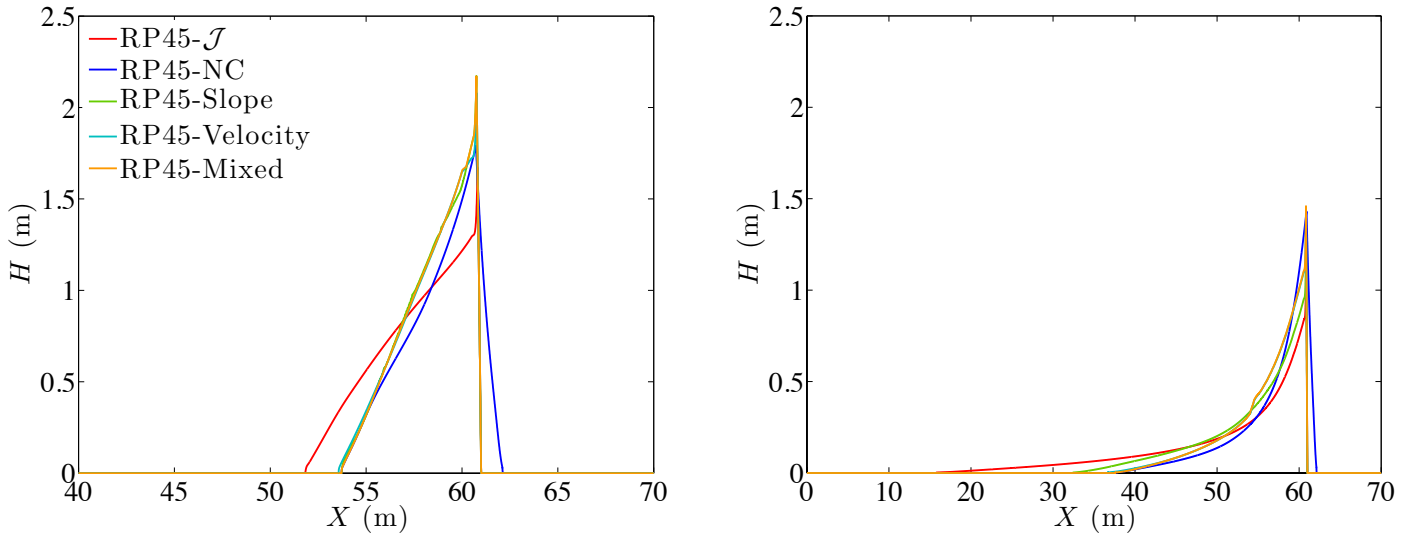

(a) $t = 1$ s (b) Solution at rest s

Figure 9: Test 1: Solutions of the RP45 model with different corrections: evolution ($\delta_0 = 52°$).

ii) To compare the deposits on the horizontal plane simulated with the different models for $\delta_0 = 30°$ ($< \arctan(3)$).

As expected, the simulations carried out with $\delta_0 \geq \arctan(3)$ reveal that the initial solution stays at rest for both the RP45-NC and RP45-$\mathcal{J}$ models. If δ_0 is slightly reduced, the granular mass should start moving. We have checked that the solution corresponding to the RP45-$\mathcal{J}$ model fulfills this condition. However, the RP45-NC model does not since the simulated granular mass stays at rest until the value of δ_0 is reduced by 20%.

Now, let us set $\delta_0 = 30°$, for which the granular mass should spread on the sloping plane and finally stop on the horizontal plane. The time evolution of the mass is shown in Figure 11 and the deposit in Figure 12. The values of the Jacobian are superimposed on the figures. In these figures, we plot $1 + H$ rather than H in order to compare the local thickness with the Jacobian, for which the reference value is 1. Note that over the inclined plane (placed at $X > 0$), we have $\widetilde{B}(X) = 0$ so $\mathcal{J} = 1 - \partial_X(H)\sin(45°)$.

At the beginning of the motion, $\partial_X(H) > 0$ in the half of the avalanche towards the front, then $\mathcal{J} < 1$. Consequently, $\mu \cdot \mathcal{J} < \mu$, so the solution of the RP45-$\mathcal{J}$ model is slightly faster than that of the RP45-NC model (see Figure 11(a)). As time increases, the front of the avalanche of the model with correction $\mathcal{J}$ is located further downslope on the inclined plane with respect to the solution of the model without correction. Nevertheless, the simulated mass obtained with both models is quite flat with $\partial_X(H) \simeq 0$. This behavior can be seen in Figure 11(b), corresponding to $t = 1.5$ s, in which the fronts of the avalanches are flowing on the final part of the inclined plane. We can also observe that in this situation $\mathcal{J} \simeq 1$, then $\mu \cdot \mathcal{J} \simeq \mu$. In this regime both models behaves in the same way, i.e. the correction plays a negligible role.

When the avalanches reach the horizontal plane (placed at $X < 0$), we have $\partial_X \widetilde{B}(X) = -1$, since the angle between the bottom and the reference plane is 45°. In fact, $\widetilde{B}$ is the most significant term in $\partial_X(\widetilde{B} + H)$ when computing the Jacobian. As a consequence, $\mathcal{J} > 1$, so $\mu \cdot \mathcal{J} > \mu$ (see Figure 11(c)).

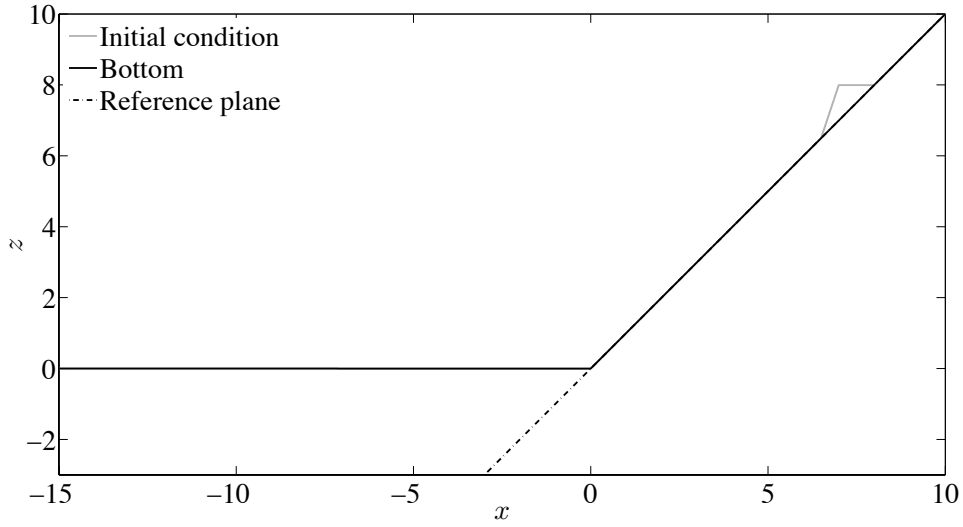

Figure 10: Test 2: Initial condition. Landslide free surface, bottom and reference plane.

This decelerates the avalanche simulated with the RP45-$\mathcal{J}$ model in such a way that it is overtaken by the one simulated with the RP-NC model. As a result, the RP45-$\mathcal{J}$ deposit is located much closer to the slope break than the RP-NC deposit, located far away (Figure 12). In this test the Jacobian reaches its maximum value when calculated on the deposit.

In Figure 13, we compare the RP45-NC and RP45-$\mathcal{J}$ deposits to the one obtained with the SHALTOP code where we have imposed $\mathcal{H} = 0$ in order to analyze the influence of the term defined by $U^2\,\mathcal{H}$ in the bed pressure correction (43). Because, SHALTOP imposes the shallow approximation and performs depth-averaging in the right direction whatever the topography, it is considered here as the reference solution [16], [5], [25]. The influence of the terms involving $\mathcal{H}$ in the models with curvature will be analyzed in Test 3. Figure 13 shows that the model with correction drastically improve the simulation of the deposit that almost coincides with SHALTOP.

Let us now compare in Figure 14 the deposits obtained with all types of corrections applied to the RP45 model as defined in Table 1 as well as the with SHALTOP with $\mathcal{H} = 0$. We observe two families of solutions: (1) those obtained using corrections (*) that set $\mathcal{C} = J_{\widetilde{B}}$ if the criterion is not fulfilled. These solutions are close to that of RP45-$\mathcal{J}$ imposing the correction $\mathcal{J}$ in all the domain; (2) those obtained by setting $\mathcal{C} = 1$ if the criterion is not fulfilled. These solutions are close to that of the RP45-NC model in which no correction is imposed at all. This reveals the importance of taking into account the value of $\widetilde{B}$ in the correction when the reference plane is not close to the bottom. As discussed above, family (1) is close to the SHALTOP simulation with $\mathcal{H} = 0$, which is very different from the solution obtained with the true curvature $\mathcal{H}$. Note also that although the slope of the bottom is singular at a point of the domain, the discretization of the bottom acts as a regularization that allows us to compute all terms of $\mathcal{H}$. This highlights the strong role of curvature even in this simple case of two inclined slope as will be detailed in Test 3.

Finally, Figure 15 shows the solutions of the RP45 model with different corrections when the avalanches are over the inclined plane (notice that $\widetilde{B}(X) = 0$ if $X > 0$). Now, apart from correc-

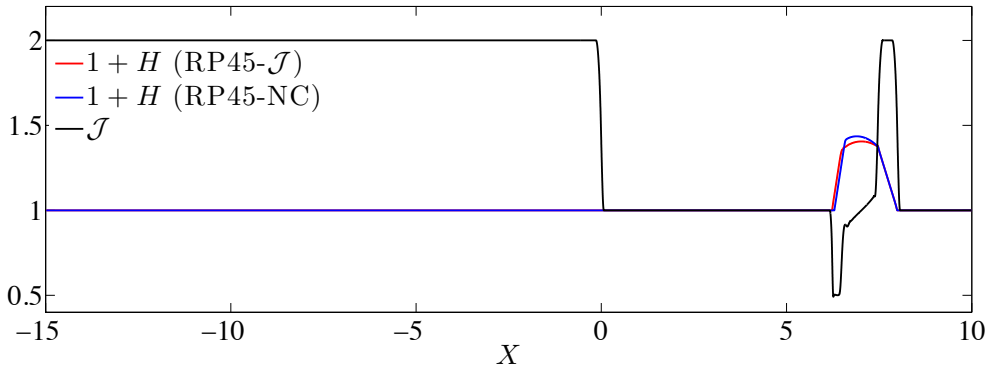

(a) $t = 0.3$ s

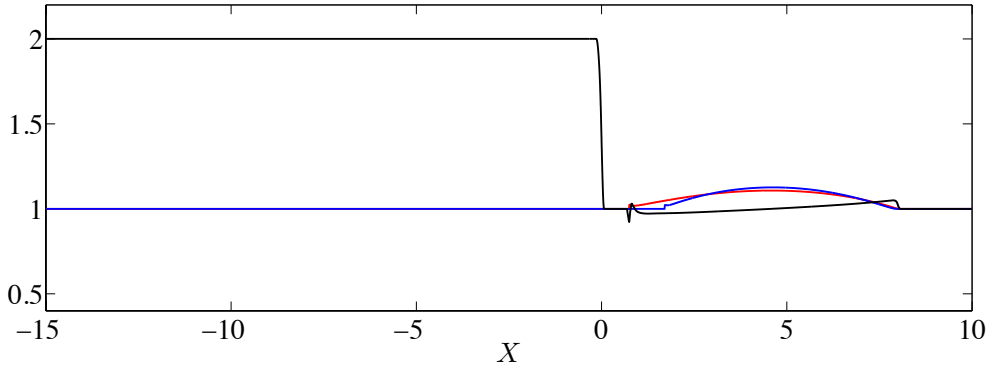

(b) $t = 1.5$ s

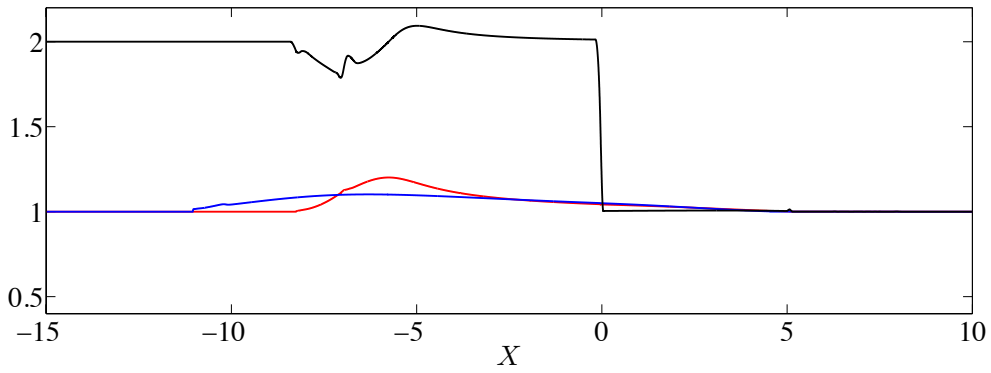

(c) $t = 3$ s

Figure 11: Test 2 on the inclined plane related to an horizontal plane: Mass thickness (added to 1 to make the visual comparison with the Jacobian easier) $1 + H$ and Jacobian related to the RP-NC and RP45-$\mathcal{J}$ models at several times ($\delta_0 = 30^o$).

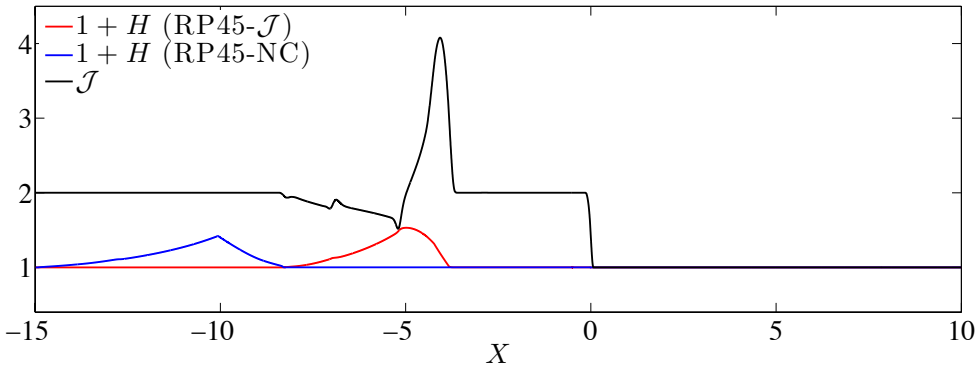

Figure 12: Test 2: Thickness of the deposit (added to 1 to make the visual comparison with the Jacobian easier) $1 + H$ and Jacobian related to the RP-NC and RP45-$\mathcal{J}$ models ($\delta_0 = 30^o$).

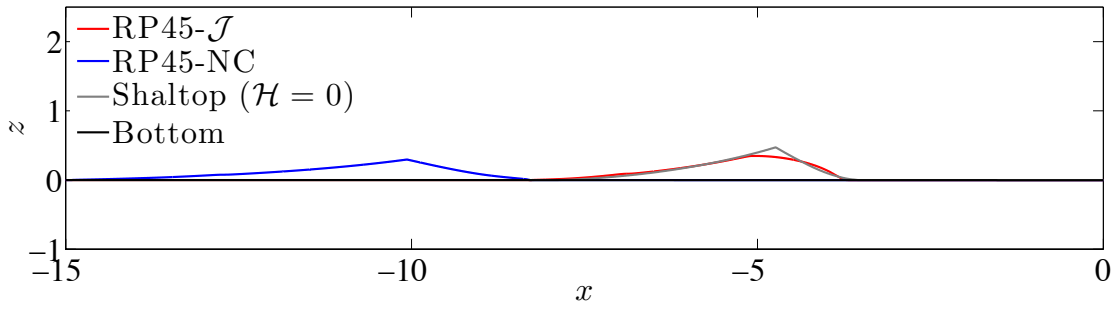

Figure 13: Test 2: Comparison between the deposits calculated with the RP45 models (with and without correction $\mathcal{J}$) and with the SHALTOP code with $\mathcal{H} = 0$ ($\delta_0 = 30^o$).

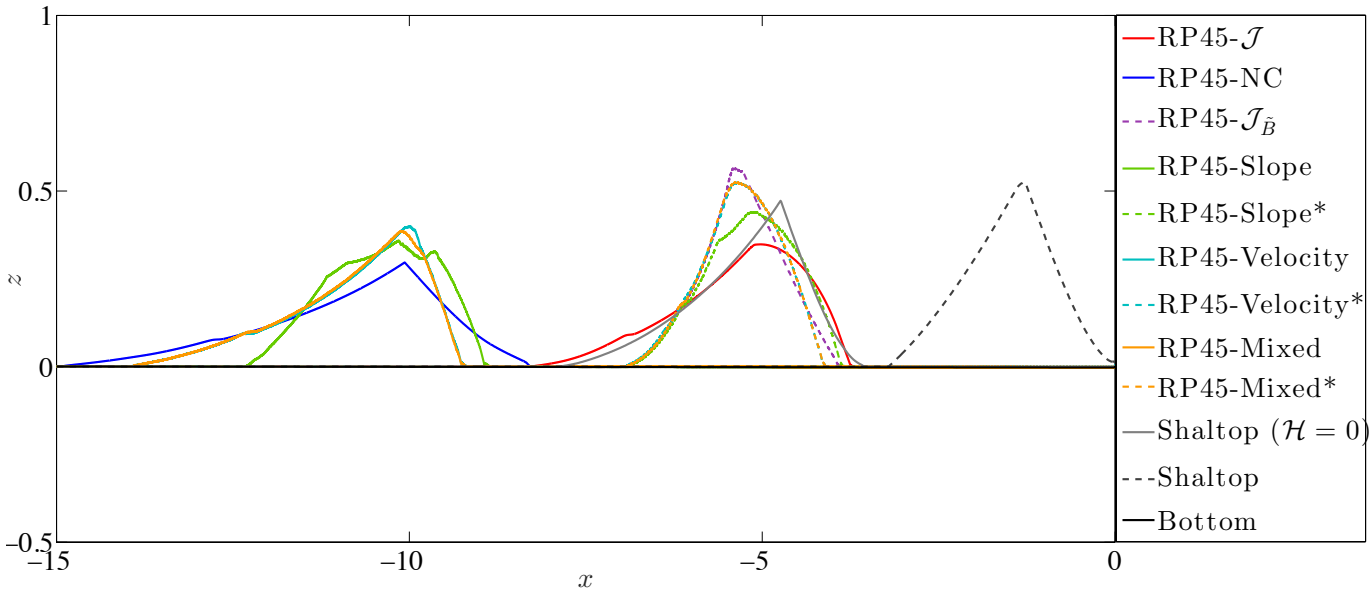

Figure 14: Test 2: Deposit simulated with the RP45 model with different corrections and comparison with the code SHALTOP ($\delta_0 = 30°$).

tion $\mathcal{J}$, the behavior of the other solutions is similar to that of the model without correction.

5.3 Test 3: Dynamics and deposits for models with curvature

The models compared in the previous tests are always defined with respect to a reference plane. In this test, we study the influence of the corrections on models taking into account the curvature of the topography. To this end, the bottom is defined as two planes with slopes 15° and 45° joined by a smooth curve. The equations for the two planes are

$$\bar{B}_1(X) = 50\tan(15°) + \tan(15°)(X-50), \quad \bar{B}_2(X) = 50\tan(15°) + \tan(45°)(X-50).$$

To design a smooth connection between the planes, the vicinity of the intersection point $(50, 50\tan(15°))$ has been replaced by an arc of circumference going from the point with abscissa $50-5\cos(15°)$ in $\bar{B}_1$ to that with abscissa $50+5\cos(45°)$ in $\bar{B}_2$ (see Figure 16). As in test 1, the initial condition is a parabolic profile given now by

$$H(X) = \max\Big(-5(X-59)(X-61),\, 0\Big)$$

The domain $X \in [0, 70]$ is discretized in 7000 cells and the CFL condition is set to 0.7. In this test we consider a Coulomb friction law with $\delta_0 = 30°$.

The thickness of the deposit simulated for the different models is compared in Figure 17. We observe that the maximum height and spread of the avalanches are different for this test in the different cases, corresponding to applying or not the friction correction and the curvature terms $\mathcal{H}$.

In Figure 17, we can observe that the cases with $\mathcal{H} = 0$ correspond in general to a smaller friction force in this test related to the modified pressure, because $\partial^2_{X^2} B > 0$. The rear position and shape of

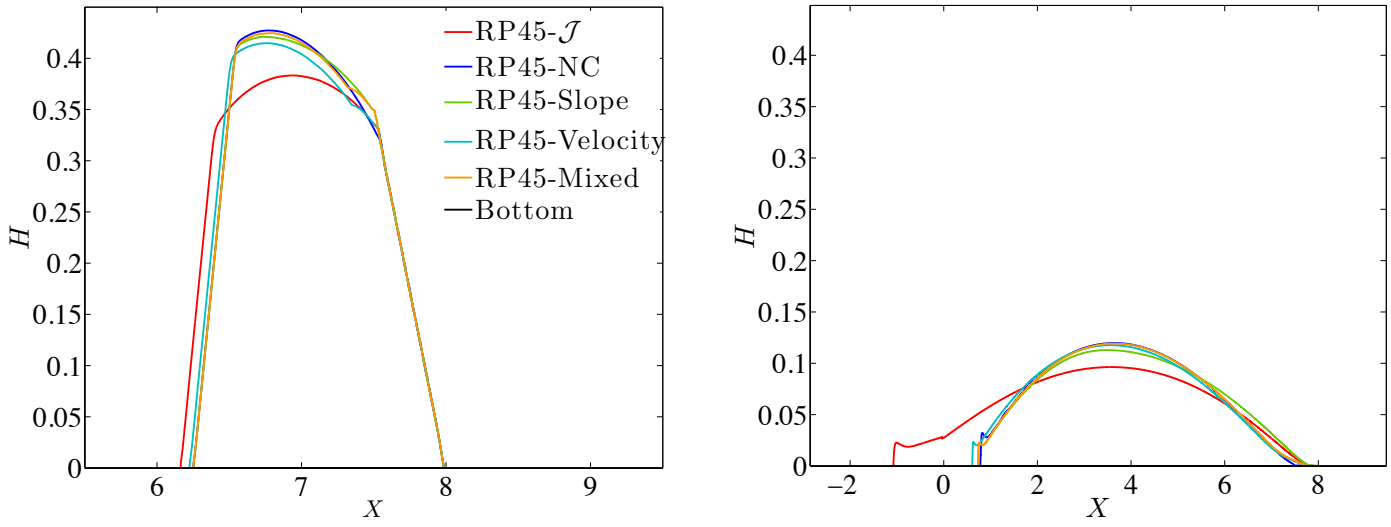

(a) $t = 0.3$ s (b) $t = 1.5$ s

Figure 15: Test 2: Solutions of the RP45 model with different corrections (evolution, $\delta_0 = 30^o$).

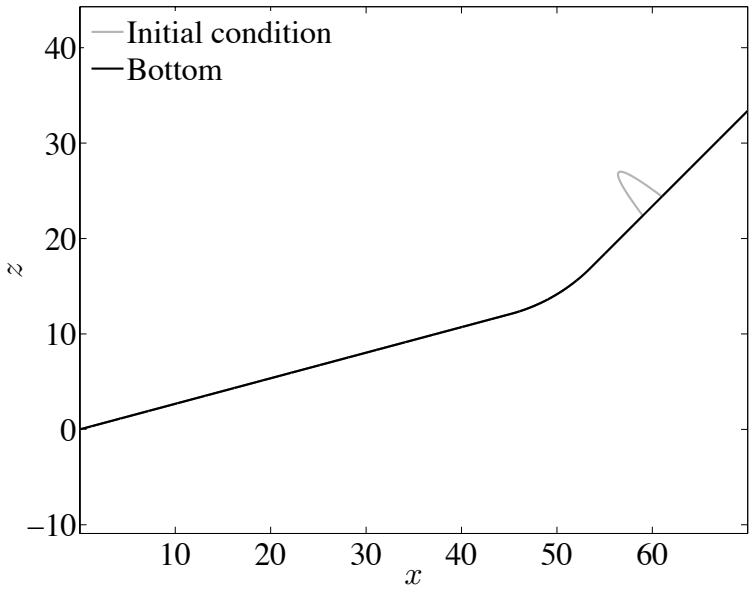

Figure 16: Test 3: Initial condition. Landslide free surface and bottom.

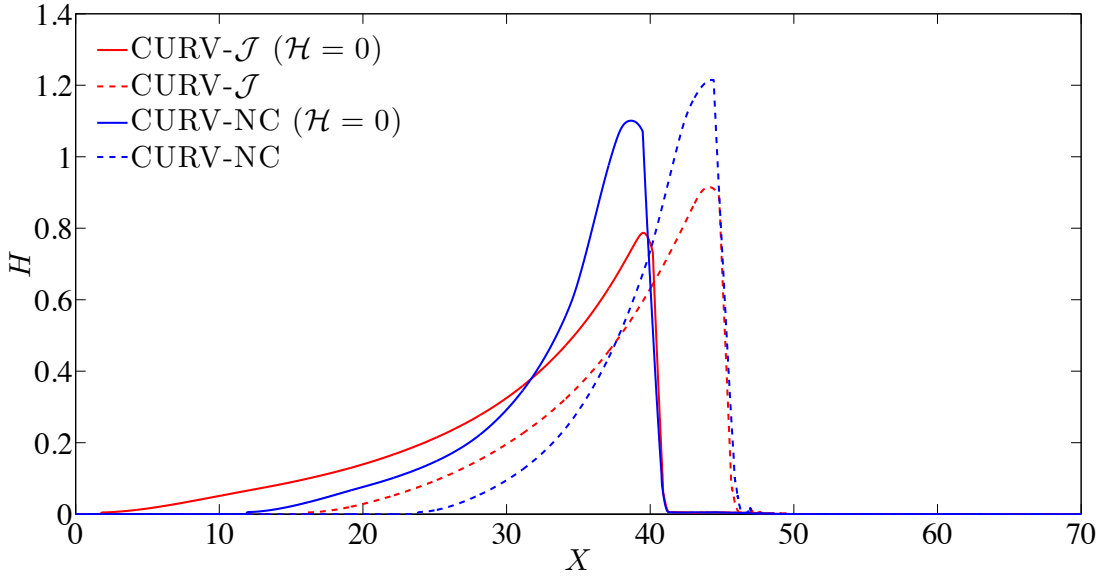

Figure 17: Test 3: Deposit. Comparison of the thickness H calculated with the CURV models with and without correction $\mathcal{J}$ ($\delta_0 = 30^o$).

the deposit are only slightly affected by the correction whether $\mathcal{H} = 0$ or not. The correction however strongly affects the frontal part of the mass, the avalanche always spreading much further for the model with correction $\mathcal{C} = \mathcal{J}$.

The value of the Jacobian at several times is presented in Figure 18. The highest values are reached at the earlier times (the continuous lines overlap the dashed lines in Figure 18a). Nevertheless, during the evolution, the Jacobian is close to 1. The discharge, $Q = HU$, is also presented in the form of $1 + Q/Q_{max}$, where Q_{max} is the maximum of Q in space and time during the simulation. We can see that at $t = 5.2$ s, a peak of the discharge coincides with an increase of the Jacobian. This is a consequence of the stopping of the avalanche at the front, which induces an accumulation of the granular mass in the rear part, as can be seen also in Figure 18b. This can also be observed on the deposit (Figure 18c) where the Jacobian is only different from about 1 near the rear of the avalanche.

Finally, Figure 19 shows the evolution in time of the front and rear of the avalanches simulated with the models with different corrections. We can observe that the rear part corresponding to the no-correction model ($\mathcal{C} = 1$) spreads upwards at the first instants (as shown in test 1) while the model with correction $\mathcal{C} = \mathcal{J}$ does not. Interestingly, for the models using a correction restricted to specific regimes (e. g. small velocity, etc.), the rear part also behaves correctly, i.e. it does not spread upwards. The front of the models corresponding to $\mathcal{C} = \mathcal{J}$ moves faster than the front simulated in all the other models, since $\partial_X(H) > 0$ (thus, $\mathcal{J} < 1$) during the whole flow, as explained in test 2. However, the front simulated with the models using a correction restricted to specific regimes is close to the front calculated with the model without any correction. This again shows the strong role of the correction all along the flow and therefore in regimes where this correction could not be valid. The model with the correction based on Mixed criteria simulates a front position closer to the one obtained without correction, while the model based on the Slope criterion is the fastest.

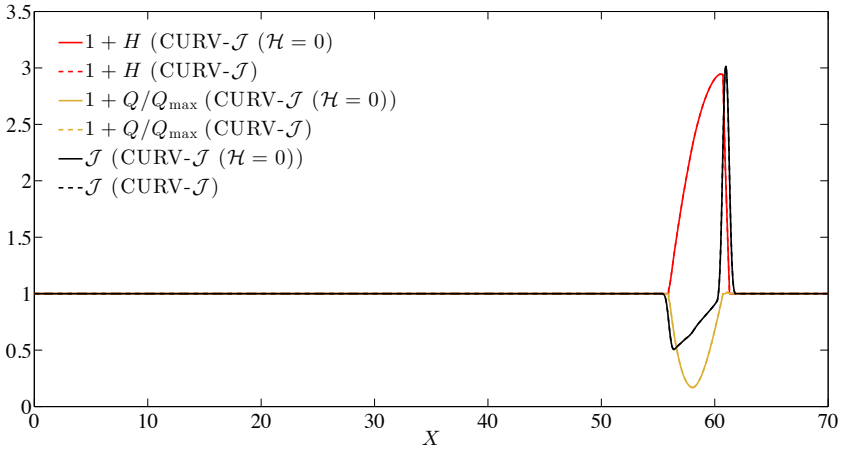

(a) $t = 0.5$ s

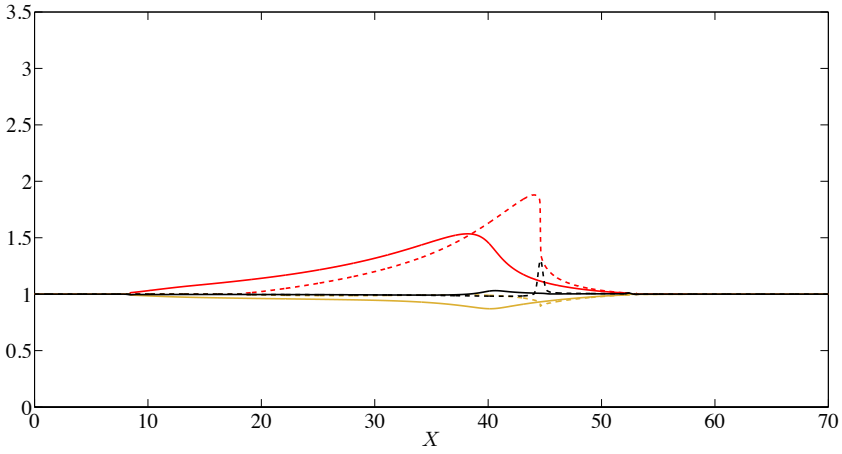

(b) $t = 5.2$ s

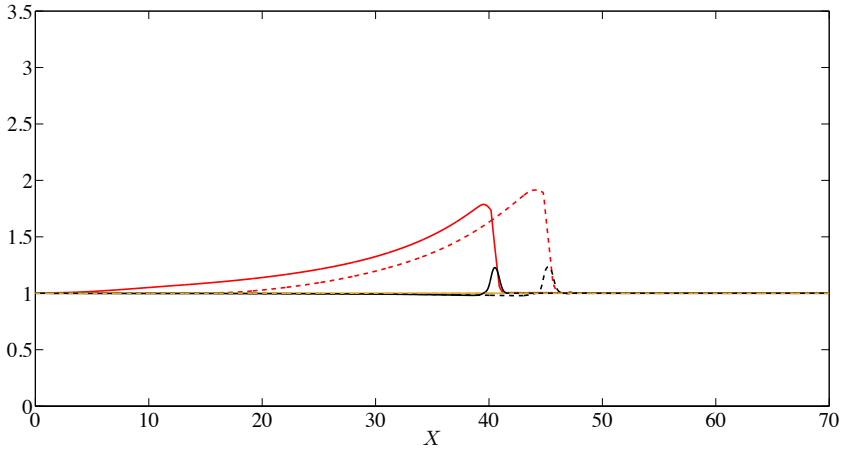

(c) Steady state

Figure 18: Test 3: Flow thickness and relative flux (added to 1 to make the visual comparison with the Jacobian easier) $1 + H$ and $1 + Q/Q_{max}$, respectively and Jacobian related to CURV-$\mathcal{J}$ ($\mathcal{H} = 0$) and CURV-$\mathcal{J}$ at several times ($\delta_0 = 30^o$). Here, $Q = HU$ and $Q_{max} = \max_{(X,t)} Q(X,t)$.

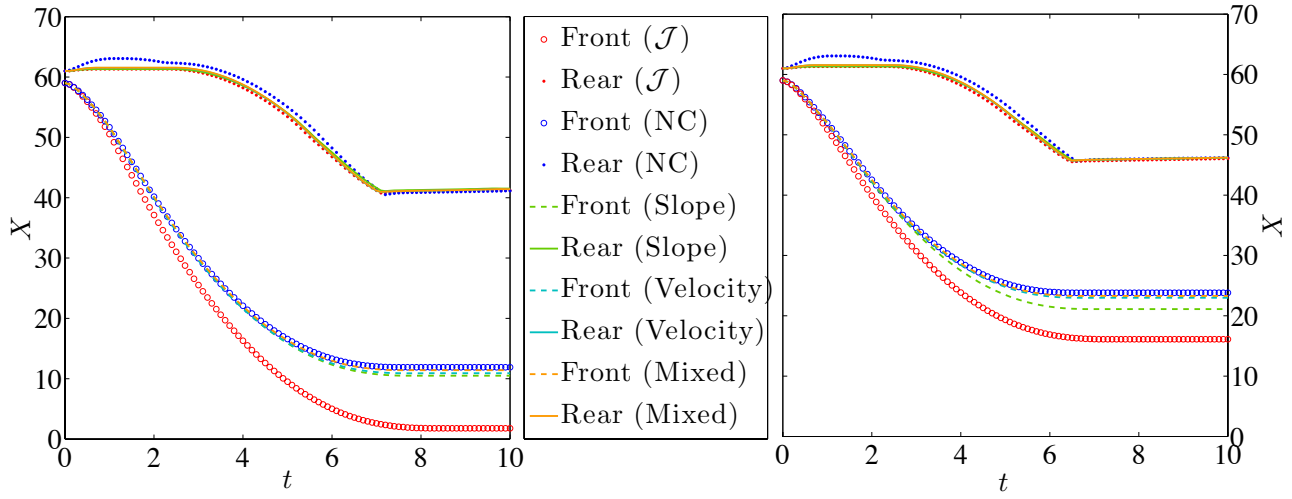

(a) CURV model ($\mathcal{H} = 0$)

(b) CURV model

Figure 19: Test 3: Evolution in time of the front and rear flow positions calculated with the CURV models with and without correction $\mathcal{J}$ ($\delta_0 = 30°$).

5.4 Test 4: Comparison with experimental data

We compare here the numerical results of the models with the data from the experiment performed by Sylvain Viroulet and presented in [26].

The experiment consisted of a release of a granular mass confined behind a removable gate in the upper part of a plane with slope α (see Figure 20 for a sketch and notation). The granular material was made up of glass beads of diameter $d_s = 4$ mm and density $\rho_s = 2500$ kg/m^3. A thin layer of these beads was stuck all along the bottom surface. The reservoir was filled with 2 kg of beads after being compacted to a compaction index of $\varphi = 0.6$.

The tank was 2.20 m long, 0.20 m large and 0.40 m high. The experiment was been carried out for a slope $\alpha = 35°$. The initial height of the granular layer was $h_{s0} = 0.249$ m, maximum at point $x_0 = 0.2199$ m (given by the location of the lifting gate). In our case, a longitudinal section was considered to perform the 1D simulation and we took the slope of the reference plane equal to the inclination $\theta = \alpha = 35°$.

The results were obtained by using 2000 points, $\Delta x = 0.001$ m and a CFL condition of 0.9. The Pouliquen friction law was considered with adapted rheological parameters since we had $d_s = 4$ mm (the diameter of the glass beads used by Pouliquen and Forterre in [3] was 0.5 mm). As in [27], we took $L = 5.2$ mm and friction angles $\delta_1 = 22.1°$, $\delta_2 = 31.8°$ and $\delta_3 = 23.3°$.

In Figure 21, we explore the evolution of the avalanches in the first stages (during the flow on the inclined plane) for the RP35 model with different corrections (note that the solutions corresponding to these models coincide with those of CURV models when the avalanche is still on the inclined plane because $\widetilde{B} = 0$). These solutions are compared with the experimental data (the curves for the experiments were obtained from digital images and kindly provided by P. Poulain (IPGP)). Solutions corresponding to the RP35-NC and RP35-Mixed* models are identical and apparently slightly closer

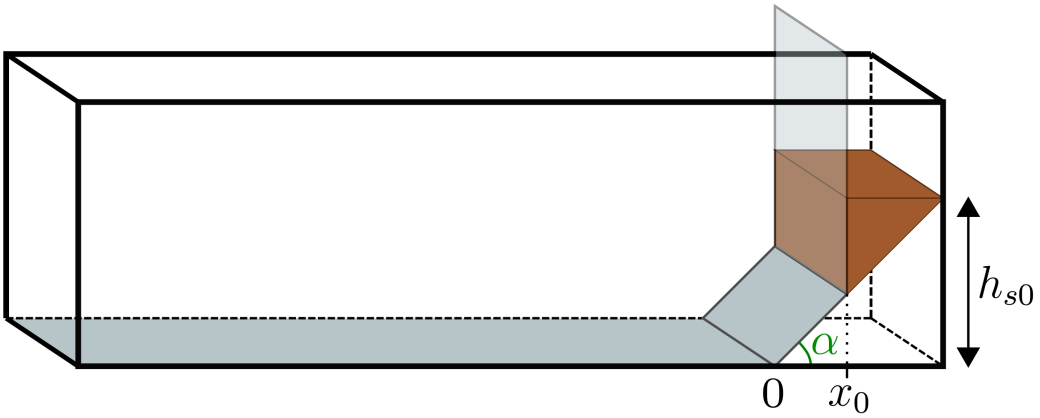

Figure 20: Test 4. Sketch of the experiment and notation. In our case, $\alpha = 35°$, $x_0 = 0.2199$ m and $h_{s0} = 0.249$ m.

to the experimental data than that of the RP35-$\mathcal{J}$ model that extends further down the slope.

Figure 22 shows the deposit simulated with the different models as well as the experimental deposit. It reveals again how different the behaviors of the RP35 models are. As in test 2, the runout of the RP35-NC model is larger than any other. The models with no curvature effects all go further than those with curvatures, in agreement with [4] (see their Figure 11). The deposits simulated with models accounting for curvature effects are all closer to the experimental deposit. They all give a similar position and shape of the rear part of the avalanche. The experimental deposit extends further upslope, possibly due to wall effects (see e.g. [13], [28]). The closest solution to experimental data for the front part is that of CURV-$\mathcal{J}$, while the runouts corresponding to the CURV-Mixed model and SHALTOP fall short.

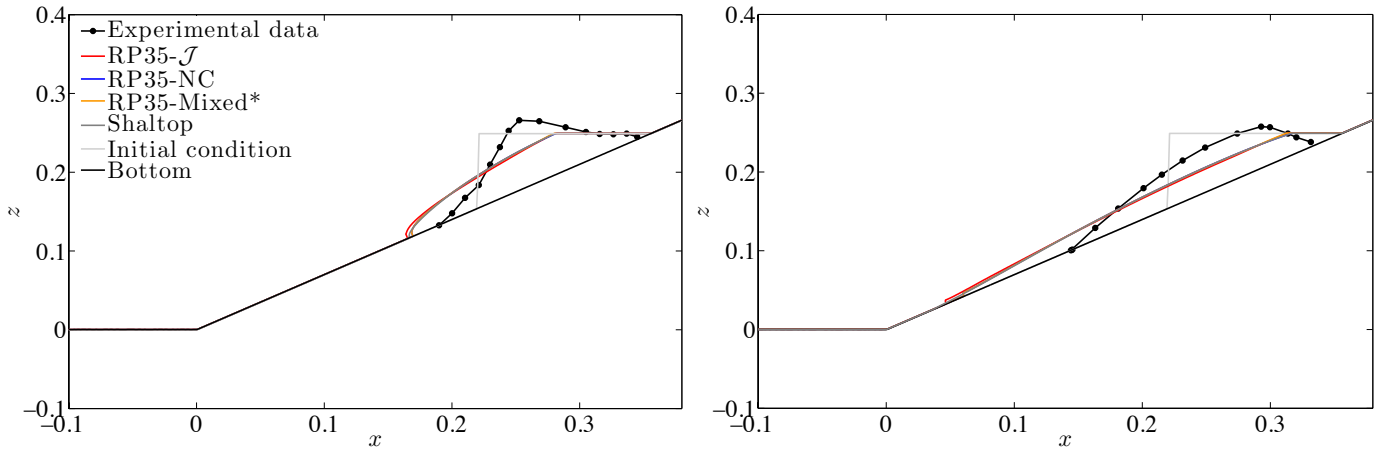

(a) $t = 0.1$ s (b) $t = 0.2$ s

Figure 21: Test 4: Evolution of the avalanches in the first stages. The solution of the model without any correction (NC) is identical to that with correction Mixed*.

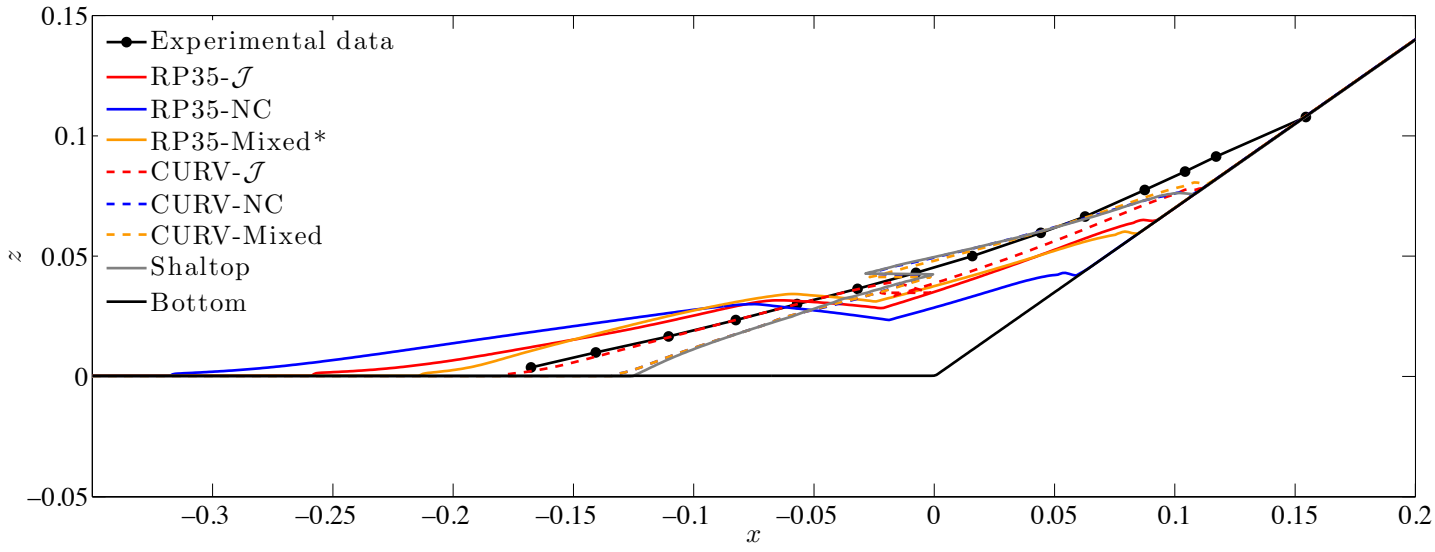

Figure 22: Test 4: Solutions at rest. Comparison of results for models considering and not considering the curvature of the bottom with experimental data. The deposit relative to the CURV-NC model is identical to that of CURV-Mixed model.

5.5 Test 5: Influence of the correction on 2D flow over an inclined plane

In this test, analogous to test 1 but in 2D, we show the influence of the basic correction $\mathcal{J}$ applied to a model with coordinates expressed in terms of a reference plane. We consider an initial parabolic granular mass released from rest on an inclined 45°-sloped plane and explore its behavior during the dynamics and the deposit for the RP45-$\mathcal{J}$ and RP45-NC models.

The bottom is given by

$$\bar{B}(X, Y) = \tan(45°)X$$

and the initial condition by

$$H(X, Y) = \max\left(-5(X - 19)(X - 21) - 5Y^2, 0\right)$$

(see Figure 23). The domain $(X, Y) \in [0, 24] \times [-8, 8]$ is discretized in 480×320 cells and the CFL condition is set to 0.7.

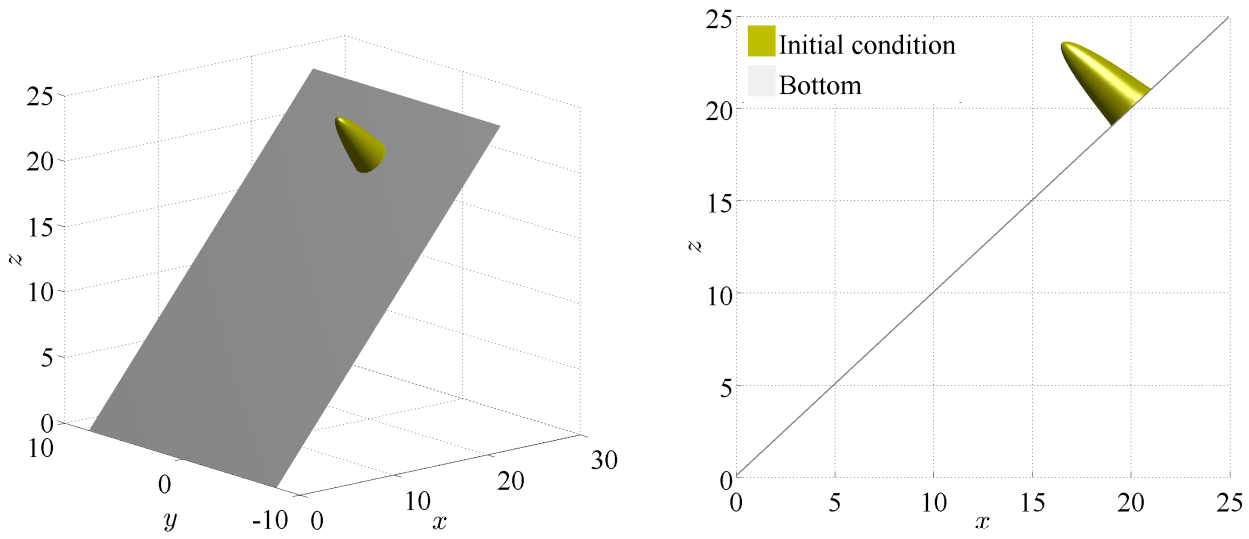

Figure 23: Test 5. Initial condition and bottom. Left: a 3D perspective. Right: a section of the initial condition at $y = 0$.

Keeping in mind that $\arctan(|\partial_x \eta|) = 36.95°$ at the rear part of the initial condition, we consider a constant friction $\mu = \tan \delta_0 = 37°$ to evaluate its motion when the surface slope is close to the friction angle. As in the 1D case, the model with correction $\mathcal{J}$ is the only one satisfying the Coulomb criterion of motion, as can be seen in Figure 24 by comparing the evolution of the level curves with the black discontinuous circular line, corresponding to the initial condition.

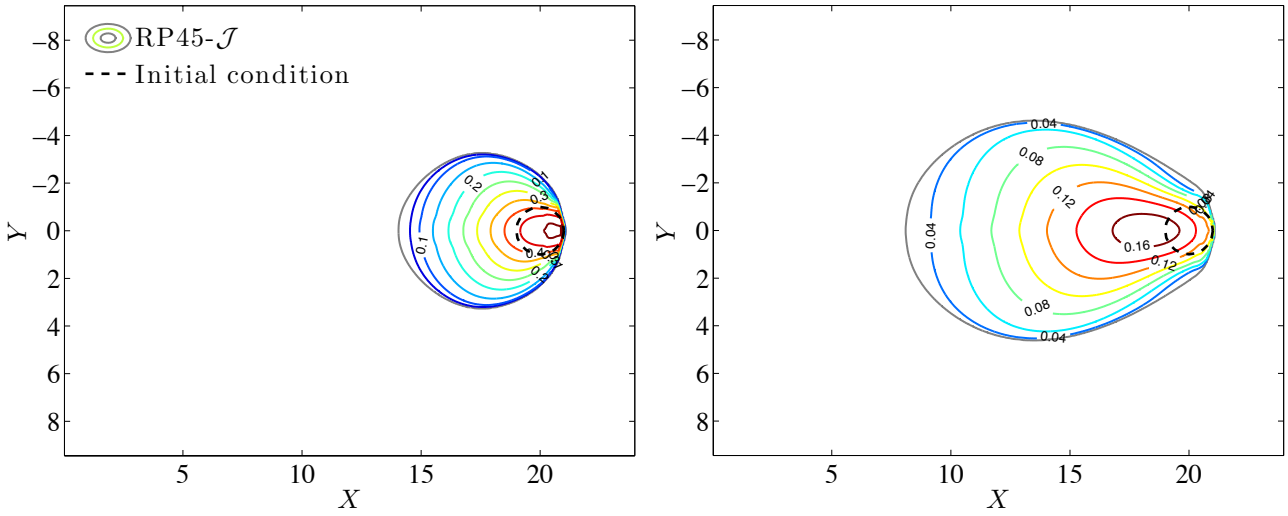

(a) Solutions for the RP45-$\mathcal{J}$ model at $t = 0.45$ s (left) and $t = 1$ s (right).

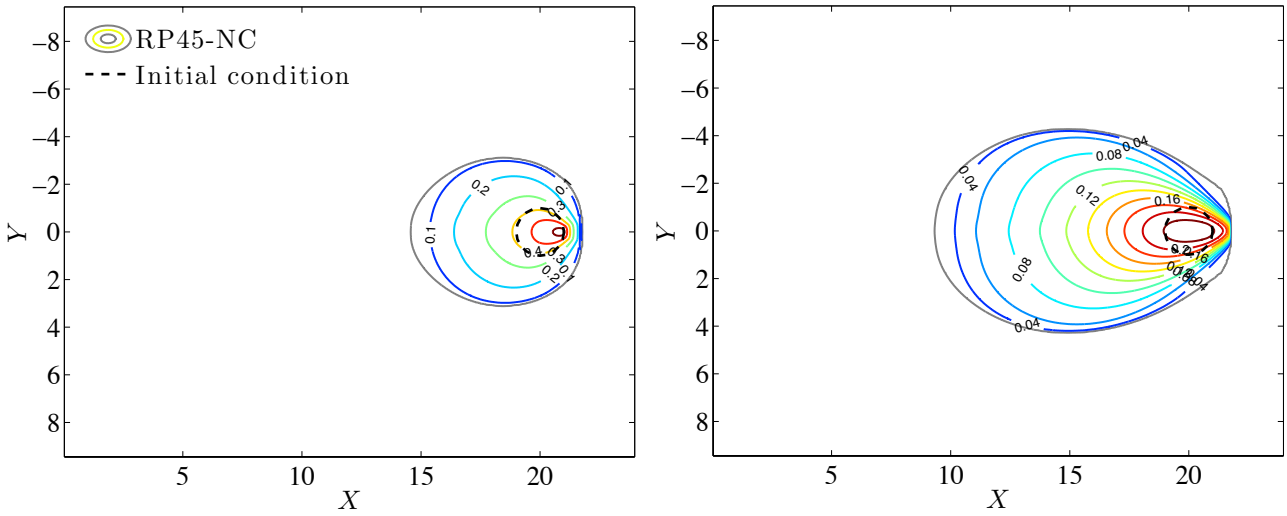

(b) Solutions for the RP45-NC model at $t = 0.5$ s (left) and $t = 1$ s (right).

Figure 24: Test 5. Evolution of the avalanches for the RP45-$\mathcal{J}$ and RP45-NC models.

5.6 Test 6: Motion threshold for 2D models with and without correction

This test could be considered as an academic complement to the previous one since it focuses again on the comparison of the RP models with and without a correction. The bottom is given using cartesian coordinates by

$$b(x, y) = \tan(20°)x$$

as well as the initial parabolic granular mass, namely,

$$\eta(x, y) = \max\left(1.5 - (x - 2.5)^2 - y^2, b(x, y)\right)$$

(see Figure 25). The domain $(X, Y) \in [1, 4] \times [-2, 2]$ is discretized in 750×1000 cells and the CFL condition is set to 0.7.

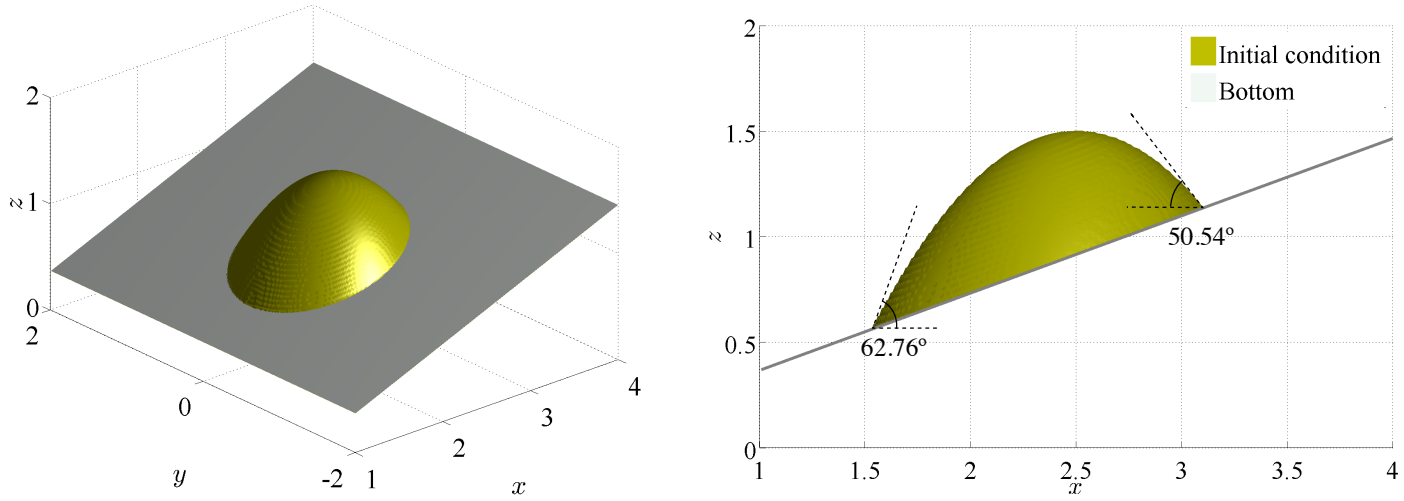

Figure 25: Test 6. Initial condition and bottom. Left: a 3D perspective. Right: a section of the initial condition when $y = 0$.

We have computed $\arctan(|\partial_x \eta|) \simeq 62.76°$ at the front part (respectively, $\arctan(|\partial_x \eta|) = 50.54°$ at the rear part) of the initial condition so, if we consider a constant friction $\mu = \tan(58°)$, motion should be detected only at the front part of the avalanche. The solution of the corrected model well reproduces these features while the solution of the RP20-NC model behaves in the opposite way as shown in Figure 26. Indeed, at the first instants ($t = 0.05$ s), motion only occurs at the rear part of the granular mass.

5.7 Test 7: 2D simulation of the Pouliquen-Forterre experiments

Now we perform a simulation to compare the numerical results of the models with the data from the experiment performed by [3]. The basic experimental set-up was the following.

The bottom was an inclined plane with slope $\theta = 23°$, made rough by gluing one layer of particles (the same material as the released mass) on the plane. A spherical cap full of these particles was placed at the top of the inclined plane and then removed (Figure 27), so that the released material started

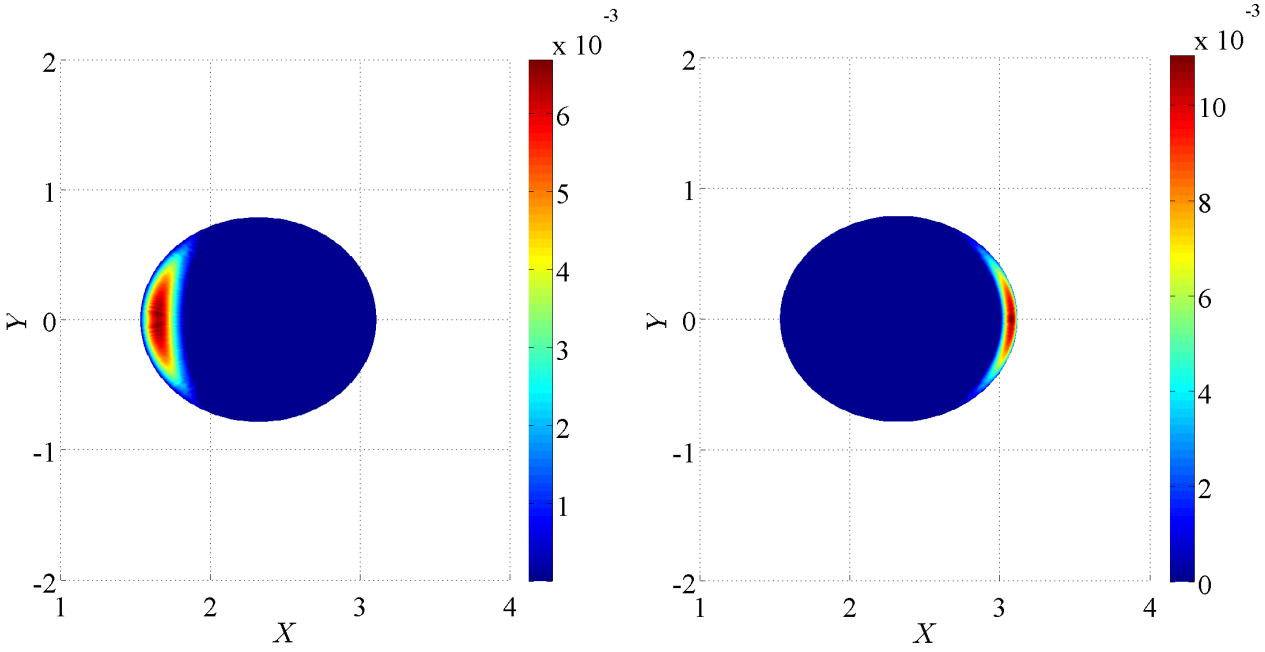

(a) RP20-$\mathcal{J}$ model. (b) RP20-NC model.

Figure 26: Test 6. Q at $t = 0.05$ s ($\delta_0 = 58°$).

to flow down the slope and finally stopped leaving a tear-shaped deposit. Figure 27 also shows the dimensions of the spherical cap used for the initial condition, i.e. $r = 0.031$ m and $R = 0.06$ m.

This simulations were obtained for a domain $(X, Y) \in [-0.05\cos(23°), \cos(23°)] \times [-0.15, 0.15]$ discretized in 960×300 (thus, the inclined plane is considered to be 1.05 m long and 0.3 m wide). The CFL condition is set to 0.9. In this test, we consider a friction coefficient $\mu = \mu_P$, where μ_P is Pouliquen's friction coefficient as described in section 1.

Figure 28 shows a comparison between the numerical solutions for both the RP23-NC and RP23-$\mathcal{J}$ models and the experimental results at several times (for more details on the experiments see [3, p. 142]). During the flow, the front part of the model with correction $\mathcal{J}$ is ahead of the front simulated with the model without correction, itself being ahead of the experimental front. The difference between the models and the experiments is smaller for the deposit. Overall the model without correction seems to better reproduce the experiments in that case. As a complement to the previous figure, the profiles of these avalanches along the plane for the cross-section located at $y = 0$ are represented in Figure 29 at the same times. Additionally, the numerical solution corresponding to the RP23-Mixed model is included, showing a behavior quite similar to that of RP23-NC. As a result, the restriction of the correction to specific regimes where it is expected to be valid makes it possible to induce only small effects during the dynamics where this correction is questionable.

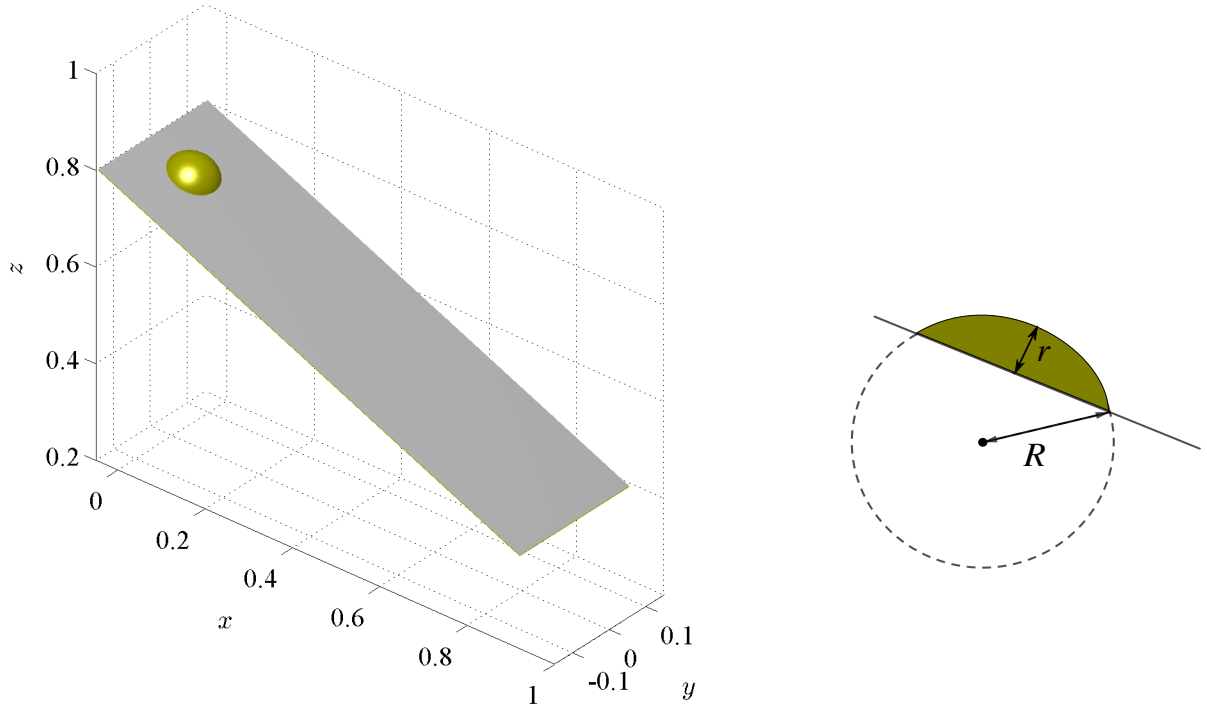

Figure 27: Test 7. Initial condition and bottom. Left: a 3D perspective. Right: a section of the initial condition at $y = 0$ on the inclined plane; cartesian coordinates x and y are equal to 0 for the point at the rear part.

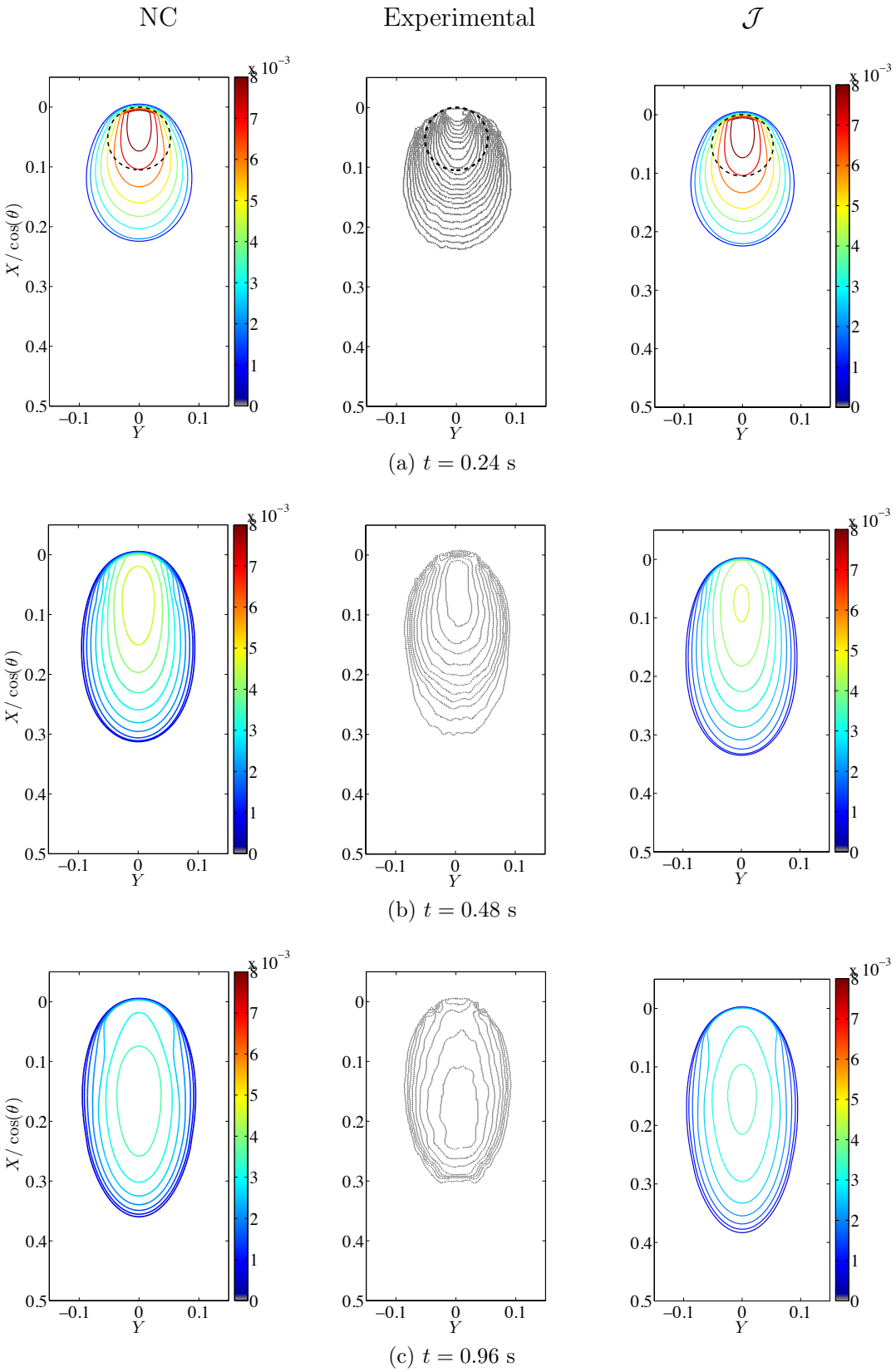

Figure 28: Test 7. Time evolution of the thickness of the granular mass. Left: the RP23-NC model. Center: experimental data (contour of constant thickness every 0.005 m). Right: the RP23-$\mathcal{J}$ model. The initial condition is represented by the dashed black line in the upper row.

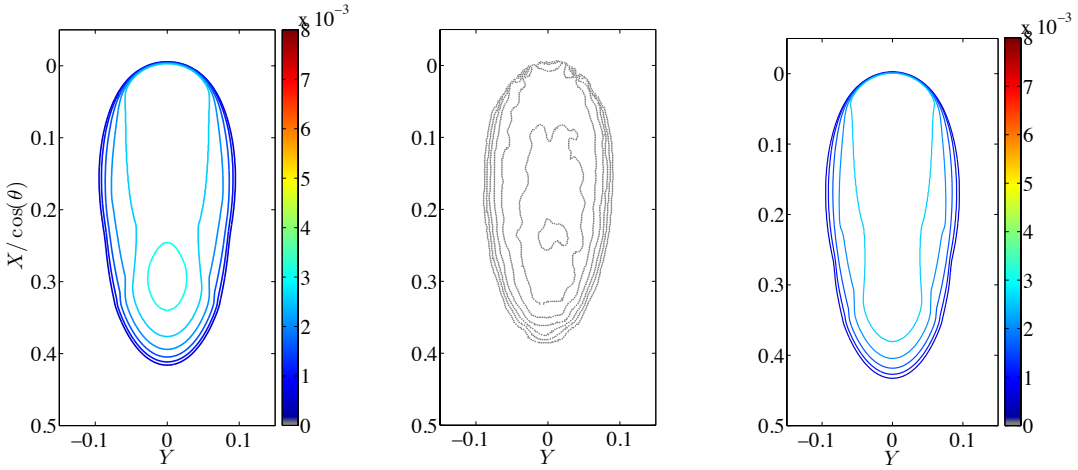

(d) $t = 2.4$ s

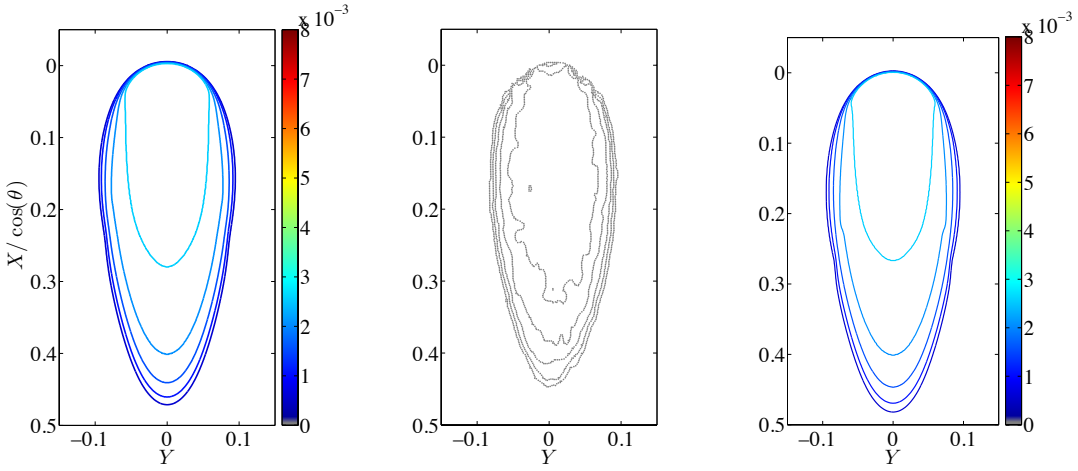

(e) $t = 6$ s

Figure 28: Continuation.

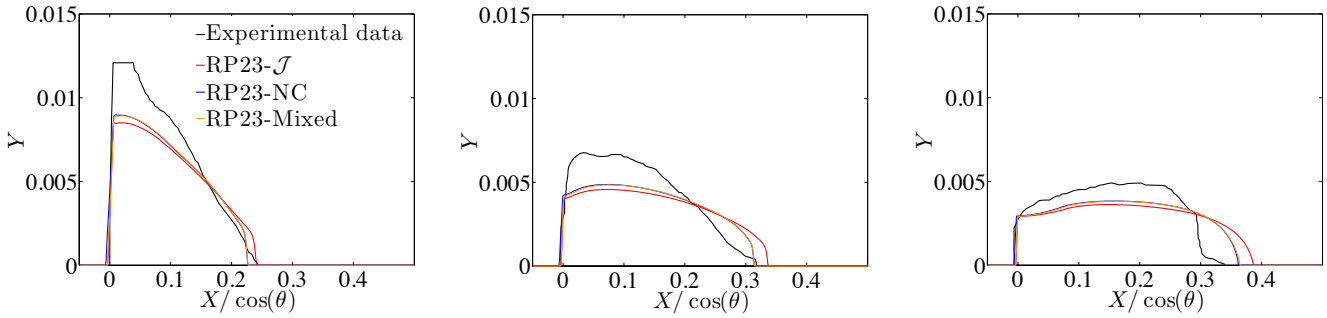

(a) $t = 0.24$ s (b) $t = 0.48$ s (c) $t = 0.96$ s

(d) $t = 2.4$ s (e) $t = 6$ s

Figure 29: Test 7. Time evolution of the thickness profiles of the granular mass along the plane at $y = 0$ for the RP23 model with NC, $\mathcal{J}$ and Mixed corrections.

5.8 Test 8: 2D simulation of the Gray-Wieland-Hutter experiments

In this final test a comparison of model results with the experimental data presented in [29] is considered. It has been frequently used as a benchmark to compare with models of granular flows (see for example [30], [25] and [31]). Details on the definition of the initial condition and the topography can be found in [32] (see Figure 30). In this test both Coulomb and Pouliquen's laws will be considered to analyze the results.

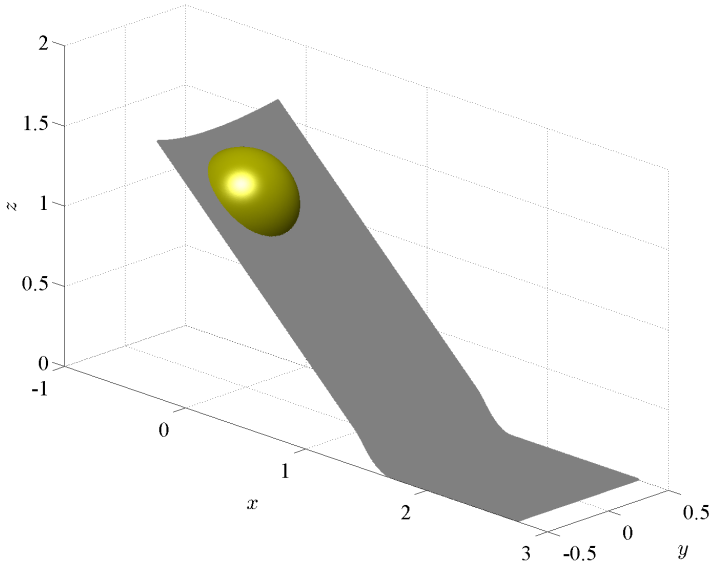

Figure 30: Test 8. Initial condition.

One of the difficulties of this test is to correctly simulate the time at which the granular flow stops, i.e., at $t = 1.79$ seconds. In [29] the authors indicate that the friction law, related to a measured friction angle of 30°, must be smaller during the simulation in the sloped part of the domain. We can observe that with the proposed correction, defined by $\mathcal{C} = \mathcal{J}$, we obtain this behavior without having to prescribe it. Indeed, $\mathcal{J} \leq 1$ in this simulation, inducing a smaller friction term than in the classical model (i.e., in the model without correction).

The results of the RP40-$\mathcal{J}$ model are presented in Figure 31. We observe that during the first instants of the simulation, up to $t = 1$ s, the mass spreads further than the experimental mass. However, at the following times, the simulation comes closer to the experimental data. The model correctly predicts the time when the flow stops and the final area of the deposit is close to that observed.

Figure 32 shows that SHALTOP (colored mass) better reproduces the mass spreading at $t = 0.51$ s with the simulated mass that travels much slower than with the RP40-Mixed* model. At $t = 1$ s, when the frontal part of the mass reaches the flat topography, the strong role of curvature can be observed in SHALTOP simulations: the simulation corresponding to the model without curvature $\mathcal{H} = 0$ (red line) moves faster than the one with curvature effects (colored mass), as observed in previous tests. In that case, the RP40-Mixed* model (black dotted lines) goes too far and SHALTOP with curvature too slowly. This difference is even more pronounced on the deposit. As the correction is not implemented in SHALTOP, it is hard to know if such a correction would improve the results. At $t = 1.79$, we can observe

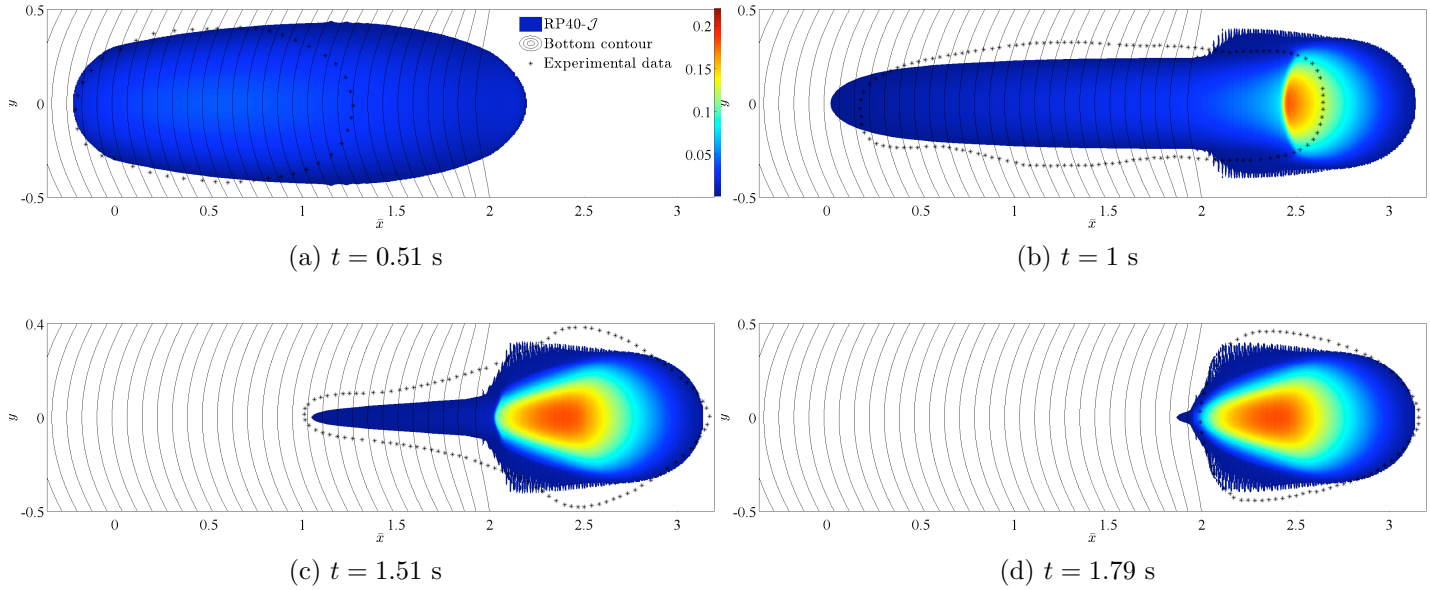

(a) $t = 0.51$ s (b) $t = 1$ s

(c) $t = 1.51$ s (d) $t = 1.79$ s

Figure 31: Test 8: Comparison of the solution of the RP40-$\mathcal{J}$ model with experimental data at several times, the latest one corresponding to the deposit (Coulomb friction law, $\delta_0 = 30°$).

that the front part of the avalanche is correctly simulated by SHALTOP when $\mathcal{H} = 0$; nevertheless, the rear part is very similar to the simulation of the model without neglecting the curvature terms. In the SHALTOP simulations (with $\mathcal{H} = 0$ and $\mathcal{H} \neq 0$) the flow has not stopped at the time observed in the experimental data.

For the sake of brevity the results corresponding to other corrections are not included. We observe that the results of the RP40-Velocity* and RP40-Slope* models are close to those of the RP40-Mixed* model. With the RP40-Velocity, RP40-Slope and RP40-Mixed models, the granular flow spreads out of the domain.

In Figure 33, we present simulations using Pouliquen's law with $\beta = 0.136$, $\gamma = 10^{-3}$, $\delta_1 = 21°$, $\delta_2 = 30.7°$, $\delta_3 = 22.2°$. For this experiment, the diameters of the particles are between 2 and 4 mm; we therefore consider $L = 1.3 \cdot 3 = 3.9$ mm. In this case we compare SHALTOP with RP40-$\mathcal{J}$. We observe that when using the proposed correction the granular mass stops at the correct time, while SHALTOP is still moving ($t = 1.79$ s). The mass simulated with RP40-$\mathcal{J}$ spreads much faster than the experiments until 1 s but then is in quite good agreement with the experimental mass. Note that this behavior was observed in test 4 when a reference plane and the proposed correction were considered. In Figures 33(e) and (f), we observe that by adding 1.5 degrees to δ_1, δ_2 and δ_3, the spreading of the avalanche is close to that of the experiment at these later times. In any case, both simulations with the RP40-$\mathcal{J}$ model give a correct stopping time.

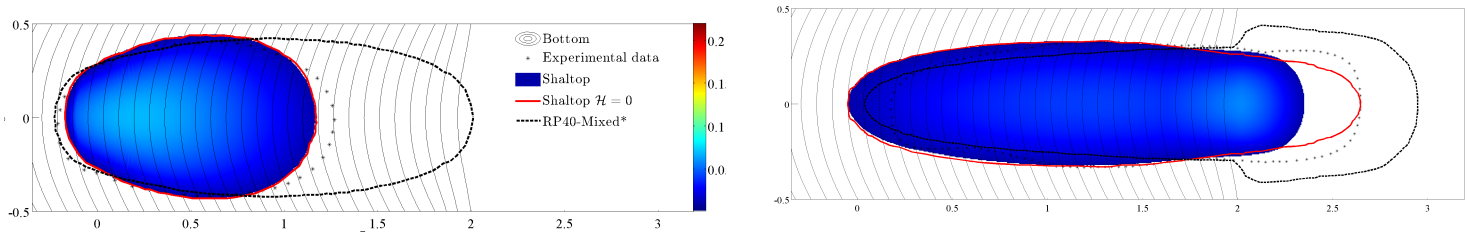

(a) $t = 0.51$ s

(b) $t = 1$ s

(c) $t = 1.51$ s

(d) $t = 1.79$ s

Figure 32: Test 8: Comparison of the solution of the SHALTOP model with experimental data and with those of the SHALTOP ($\mathcal{H} = 0$) and RP40-Mixed* models (Coulomb friction law, $\delta_0 = 30°$).

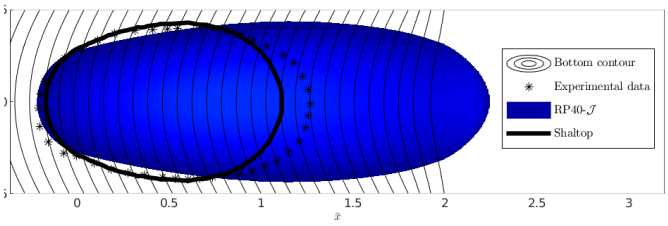

(a) $t = 0.51$ s

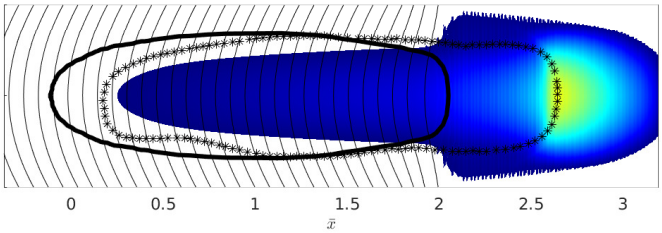

(b) $t = 1$ s

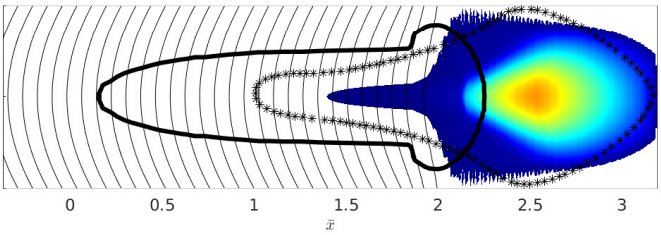

(c) $t = 1.51$ s

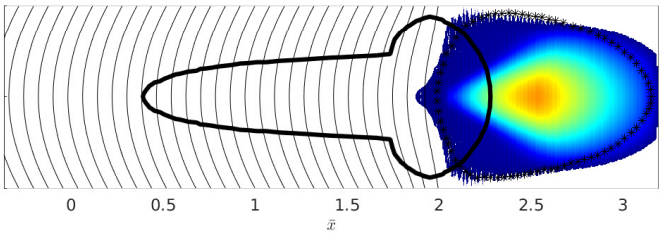

(d) $t = 1.79$ s

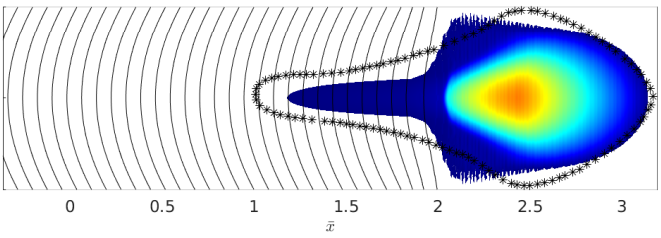

(e) $t = 1.51$ s ($\delta_i + 1.5$, $i = 1, 2, 3$)

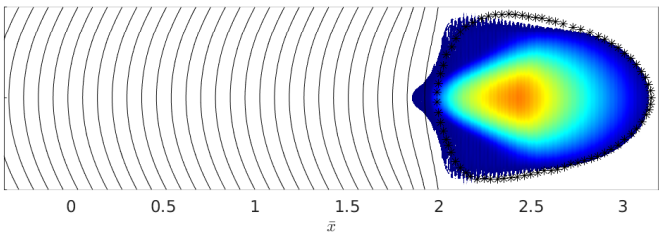

(f) $t = 1.79$ s ($\delta_i + 1.5$, $i = 1, 2, 3$)

Figure 33: Test 8: Comparison of the solution of the SHALTOP model (black line) with experimental data and with those of the RP40-$\mathcal{J}$ model (Pouliquen friction law, $L = 3.9$ mm, $\gamma = 10^{-3}$, $\delta_1 = 21^c irc$, $\delta_2 = 30.7°$, $\delta_3 = 22.2°$). Figures (e) and (f) correspond to the solution of the RP40-$\mathcal{J}$ model adding 1.5 degrees to δ_1, δ_2 and δ_3.

Conclusions

We propose here a correction of the friction term for depth-averaged shallow models. This correction is introduced in depth-averaged models in which the direction of integration is orthogonal to some reference non-flat plane or to a general bottom, taking into account curvature terms. It has been obtained by defining the friction bed term in such a way that the model well reproduces the physical threshold of motion and therefore preserves solutions at rest. It is shown that this correction could be interpreted as a second order approximation of the bed pressure for slow flows, thus going further than the leading order approximation of a hydrostatic pressure. As a consequence, the proposed modification of the friction term may be meaningful only when the flow is close to the stopping phase or exactly static. Indeed, in other regimes, the additional terms related to a higher order shallow approximation will co-exist with other second order terms related to inertia or to the visco-plastic rheology of the granular material involved.

To highlight the problem of models without correction and to quantify the effect of the proposed corrections in different regimes, a series of 8 tests have been performed by simulating granular flows in various configurations. In particular different types of criteria, on the slope or on the flow velocity, have been tested, in order to apply the proposed correction only in certain regimes: for slow flows or when the slope computed by the model without correction is not in some of the pathological situations described in section 3.

We show several examples in which classical models fail to preserve the solutions at rest by predicting a mass motion (or mass stopping) when the physical threshold of motion is not (or is) fulfilled. The proposed correction, while not completely satisfactory in all regimes, makes it possible to eliminate these misbehaviors. Three comparisons of simulated solutions with experimental data are presented. In the first, corresponding to a 1D problem, we observe that the proposed correction improves the results. In the second case, we observe that the results are analogous to the case of the model without any correction, because the flow is nearly uniform. In the last comparison, we show that the 2D model written on a reference plane with the proposed correction is the only one that correctly captures the time at which the avalanche stops, with good agreement of the spreading area of the granular flow at final times. However, the correction is shown to have a significant impact in the dynamic regime where its validity is questionable. This could be the reason why, except for the starting and stopping phases, this correction does not clearly improve the simulation results. More advanced corrections including other second order terms in the equations of mass and momentum should be developed to fully address this issue.

Acknowledgements

This research has been partially supported by the Spanish Government and FEDER through the research project RTI2018-096064-B-C22, and by the ERC contract ERC-CG-2013-PE10-617472 SLIDE-QUAKES.

References

[1] S. B. Savage and K. Hutter. The motion of a finite mass of granular material down a rough incline. *Journal of Fluid Mechanics*, 199:177–215, 1989.

[2] B. Andreotti, Y. Forterre, and Pouliquen O. *Les milieux granulaires. Entre fluide et solide*. EDP Sciences, 2011.

[3] O. Pouliquen and Y. Forterre. Friction law for dense granular flows: application to the motion of a mass down a rough inclined plane. *Journal of Fluid Mechanics*, 453:133–151, 2002.

[4] A. Mangeney-Castelnau, J.P. Vilotte, M. O. Bristeau, B. Perthame, F. Bouchut, C. Simeoni, and S. Yerneni. Numerical modeling of avalanches based on saint venant equations using a kinetic scheme. *Journal of Geophysical Research*, 108((B11) 2527), 2003.

[5] A. Mangeney, F. Bouchut, N. Thomas, J.P. Vilotte, and M. O. Bristeau. Numerical modeling of self-channeling granular flows and of their levee-channel deposits. *Journal of Geophysical Research*, 112(F02017), 2007.

[6] GDR MiDi. On dense granular flows. *Eur. Phys. J.*, E(14):341–365, 2004.

[7] P. Jop, Y. Forterre, and O. Pouliquen. A constitutive law for dense granular flows. *Nature*, 441(7094):727–730, 2006.

[8] F. da Cruz. Ecoulements de grains secs: frottement et blocage. Master's thesis, Thèse de l'Ecole Nationale des Ponts et Chaussées, 2004.

[9] O. Pouliquen. Scaling laws in granular flows down rough inclined planes. *Phys. Fluids*, 11((3)):542–548, 1999.

[10] Jop P., Forterre Y., and Pouliquen O. Crucial role of sidewalls in granular surface flows: consequences for the rheology. *J. Fluid Mech.*, 541:167–192, 2005.

[11] R Delannay, A Valance, A Mangeney, O Roche, and P Richard. Granular and particle-laden flows: from laboratory experiments to field observations. *Journal of Physics D: Applied Physics*, 50(5):053001, 2017.

[12] J. Garres-Díaz, E.D. Fernández-Nieto, A. Mangeney, and T. Morales de Luna. A weakly non-hydrostatic shallow model for dry granular flows. *Journal of Scientific Computing*, 86:25, 2021.

[13] N. Martin, I. R. Ionescu, A. Mangeney, F. Bouchut, and M. Farin. Continuum viscoplastic simulation of a granular column collapse on large slopes: $\mu(i)$ rheology and lateral wall effects. *Physics of Fluids*, 29(1):013301, 2017.

[14] A. Mangeney-Castelnau, F. Bouchut, J. P. Vilotte, E. Lajeunesse, A. Aubertin, and M. Pirulli. On the use of saint venant equations to simulate the spreading of a granular mass. *Journal of Geophysical Research: Solid Earth*, 110(B9), 2005.

[15] F. Bouchut, I. Ionescu, and A. Mangeney. An analytic approach for the evolution of the static-flowing interface in viscoplastic granular flows. *Commun, Math. Sci.*, 14(8):2101–2126, 2016.

[16] F. Bouchut and M. Westdickenberg. Gravity driven shallow water models for arbitrary topography. *Commun, Math. Sci.*, 2:359–389, 2004.

[17] J.M. Delgado-Sánchez, F. Bouchut, E.D. Fernández-Nieto, A. Mangeney, and G. Narbona-Reina. A two-layer shallow flow model with two axes of integration, well-balanced discretization and application to submarine avalanches. *Journal of Computational Physics*, 406:109186, 2020.

[18] S. B. Savage and K. Hutter. The dynamics of avalanches of granular materials from initiation to runout. part i: Analysis. *Acta Mechanica*, 86(1):201–223, Mar 1991.

[19] F. Bouchut, E.D. Fernández-Nieto, A. Mangeney, and P.Y. Lagrée. On new erosion models of savage-hutter type for avalanches. *Acta Mechanica*, 199(1):181–208, 2008.

[20] Oscar Castro-Orgaz, Kolumban Hutter, Juan V. Giraldez, and Willi H. Hager. Nonhydrostatic granular flow over 3-d terrain: New boussinesq-type gravity waves? *Journal of Geophysical Research: Earth Surface*, 120(1):1–28, 2015.

[21] L. Moretti, A. Mangeney, Y. Capdeville, E. Stutzmann, C. Huggel, D. Schneider, and F. Bouchut. Numerical modeling of the mount steller landslide flow history and of the generated long period seismic waves. *Geophysical Research Letters*, 39(16), 2012.

[22] L. Moretti, K. Allstadt, A. Mangeney, Y. Capdeville, E. Stutzmann, and F. Bouchut. Numerical modeling of the mount meager landslide constrained by its force history derived from seismic data. *Journal of Geophysical Research: Solid Earth*, 120(4):2579–2599, 2015.

[23] F. Bouchut, A. Mangeney, B. Perthame, and J.P. Vilotte. A new model of saint venant and savage-hutter type for gravity driven shallow water flows. *Comptes Rendus Mathematique*, 336(6):531 – 536, 2003.

[24] M. Brunet, L. Moretti, A. Le Friant, A. Mangeney, E.D. Fernández-Nieto, and F. Bouchut. Numerical simulation of the 30–45 ka debris avalanche flow of montagne pelée volcano, martinique: from volcano flank collapse to submarine emplacement. *Natural Hazards*, 87(2):1189–1222, Jun 2017.

[25] Marc Peruzzetto, Anne Mangeney, Francois Bouchut, Gilles Grandjean, Clara Levy, Yannick Thiery, and Antoine Lucas. Topography curvature effects in thin-layer models for gravity-driven flows without bed erosion. *Journal of Geophysical Research: Earth Surface*, 126(4):e2020JF005657, 2021.

[26] P. Poulain. Granular flows simulation and application to volcanic flank collapse. Master's thesis, Master GEO3: Risques Naturels Telluriques, 2017.

[27] P. Poulain, A. Le Friant, A. Mangeney, S. Viroulet, E.D. Fernández-Nieto, M.J. Castro Díaz, M. Peruzzetto, G. Grandjean, F. Bouchut, R. Pedreros, and Komorowski J-C. Performance and limits of a shallow model for landslide generated tsunamis: from lab experiments to simulations of flank collapses at la montagne pelée (martinique). *Preprint*, 2021.

[28] E.D. Fernández-Nieto, J. Garres-Díaz, A. Mangeney, and G. Narbona-Reina. 2d granular flows with the $\mu(i)$ rheology and side walls friction: A well-balanced multilayer discretization. *Journal of Computational Physics*, 356:192 – 219, 2018.

[29] Wieland M. Hutter K. Gray, J.M.N.T. Gravity-driven free surface flow of granular avalanches over complex basal topography. *Proc. R. Soc. Lond. Ser. A Math. Phys. Eng. Sci.*, 455:1841–1874, 1999.

[30] Crosta G.B. Lee C.F. Chen, H. Erosional effects on runout of fast landslides, debris flows and avalanches: a numerical investigation. *Géotechnique*, 56(5):305–322, 2006.

[31] Bristeau M.-O. Mangeney A. Scavia C. Pirulli, M. The effect of earth pressure coefficients on the runout of granular material. *Environ. Model. Softw.*, 22:1437–1454, 2007.

[32] Gray J.M.N.T.-Hutter K. Wieland, M. Channelized free-surface flow of cohesionless granular avalanches in a chute with shallow lateral curvature. *J. Fluid Mech.*, 392:73–100, 1999.